VOLUME 3 NUMBER 1 2010

TRANSACTIONS ON TRANSPORT SCIENCES

Ministry of Transport

CZECH TECHNICAL UNIVERSITY

TRANSACTIONS ON TRANSPORT SCIENCES

Publisher: *Ministry of Transport*, nábř. L. Svobody 1222/12, 110 15 Praha 1, Czech Republic
E-mail: *info@transportsciences.org*
URL: *www.transportsciences.org*

Editorial Office: Olga Krištofíková
Hedvika Kovandová
Jana Zelinková
Vladimír Adamec
Petr Polanský
Irena Zedková

Periodicity: Quarterly
Language: English
Scope: International scientific journal for transport sciences
Print version: ISSN 1802-971X
On-line version: ISSN 1802-9876
Registration Number: MK EČ E 18012

Each paper in the journal is evaluated by two reviewers under the supervision of the International Editorial Board.

The Research and Development Council of the Government of the Czech Republic indexed this journal in the Title List of Peer-Reviewed Journals.

Distributor: CDV – Transport Research Centre, Líšeňká 33a, 636 00 Brno, Czech Republic, journal@cdv.cz.

Study of the Development of Cracks Accompanying Mechanical Loading of Solids

P. Koktavý*
Brno University of Technology, Faculty of Electrical Engineering and Communication Technologies, Department of Physics, Brno, Czech Republic
** Corresponding author: koktavy@feec.vutbr.cz*

B. Koktavý
Brno University of Technology, [2]Faculty of Civil Engineering, Department of Physics, Brno, Czech Republic

DOI: 10.2478/v10158-010-0001-5

ABSTRACT: The formation of cracks in mechanically loaded insulators is accompanied by the generation of an electromagnetic field. Four basic processes of the crack's growth have been suggested based on the dipole model of a crack. A differential equation describing the transformation of the crack's primary parameters into a measurable electric signal has been derived for each of the four cases. Thus obtained theoretical curves have been compared with the experimental ones. Based on the comparison, some primary parameters of the crack have been determined.

KEY WORDS: Electromagnetic emission, crack, electric charge, model.

1 INTRODUCTION

The phenomenon of electromagnetic emission (EME) from solids (Koktavý, 2009) is based on the generation of an electromagnetic field arising from the mechanical excitation of the solid in question. This phenomenon may be triggered, for example, by external pressure, tensile, bending, shearing force, shocks, drilling, scratching, crushing, material fibre cutting, etc. At present, the EME waves are observed to be emitted from any material media: not only from solids, but also from liquids, gases, geological and biological objects. Measurement of electromagnetic emission signals can be employed in diagnosing these solids in the course of mechanical loading.

This paper presents a study of electromagnetic emission signals emitted from *extren 500*, an electrically non-conductive material. This material's structure is formed by a fibre-glass reinforcement bonded by a resin binder. Our specimens have been prepared in the form of rectangular blocks of dimensions (6 to 10) mm × 50 mm × 60 mm.

2 MODELS FOR THE GENERATION OF EME

Although there are currently a number of experimental studies dealing with various aspects of the electromagnetic emission phenomenon, the physical origin of this phenomenon has not been satisfactorily accounted for until now. Several models based on the assumption that mechanical loading of electrically non-conducting solids results in non-uniform distribution of electric charges on the crack faces have been presented. Opposite sign charges

occur on these crack faces, producing a time variable electric dipole or quadrupole, which in turn creates a source of EME emission. The fact that electric charges occur on the faces of a crack in the course of its formation has not been satisfactorily explained until now. The above-mentioned theory of EME generation has been submitted in many papers, for example in (Chatiašvili,1988), (Chatiašvili, 1991), (Šikula et al. 1996) and (Lokajíček & Šikula,1996).

Another model for the EME generation has been put forward by Gershenzon et al (Gershenzon et al. 1987), who suppose that electric charges are generated on the top of the crack and, moreover, the crack faces are charged with opposite sign charges. If the crack grows in size, the dipole moment changes and EME is generated.

Other models are based on physical characteristics of the displacement of dislocations. In the case of a non-homogeneous distribution of dislocations, which is due to elastic-plastic transitions accompanying a compression, the movement of the dislocation is stopped suddenly and, consequently, conductivity electrons will generate EME [6]. Still other theories are based on the growth of the dislocation length which in turn results in the growth of the dipole moment associated with the dislocation in question and, consequently, electromagnetic radiation.

Our model of EME generation is based on the hypothesis that electric charges giving rise to an electric dipole or quadrupole, occur on the crack faces.

3 CAPACITANCE SENSOR

For laboratory measurements of the electromagnetic emission, one can take advantage of a capacitance sensor in the form of a parallel-plate capacitor whose dielectric is the mechanically loaded specimen [1], see Fig. 1. Here, C is the capacitance of the pick-up capacitor; $\boldsymbol{E}$ is the intensity of the electric field in the space between the capacitor plates. The C_2R_1 circuit forms a low-pass filter, C_1 is the preamplifier input plus the cable capacity and R_1 is the equivalent resistance of the load resistance R being connected in parallel to the input resistance of the pre-amplifier.

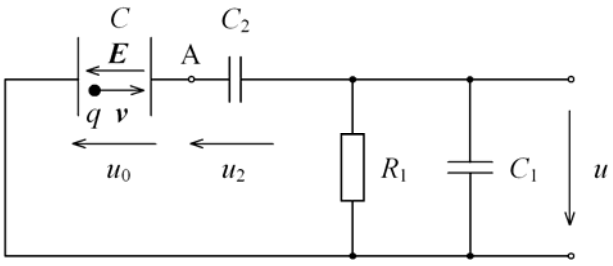

Figure 1: Capacitance sensor.

Let charges $q(t)$ a $-q(t)$ move in the space between the pick-up capacitor with velocities $\boldsymbol{v}(t)$ and $-\boldsymbol{v}(t)$, respectively. Then a differential equation for the sensor output voltage u holds:

$$\frac{\mathrm{d}u}{\mathrm{d}t} + \frac{u}{R_1 C'} = Bq(t)v(t)\,, \tag{1}$$

where $B = 2\cos\alpha/(C''d)$, $C' = C_1 + C\,C_2/(C + C_2)$, $C'' = C + C_1 + C_1\,C/C_2$, d is the specimen thickness and is an angle between $\boldsymbol{E}$ and $\boldsymbol{v}$.

In our sensor, the capacitances are as follows: C = 18 pF, C_1 = 18 pF, C_2 = 120 pF and the resistance R_1 = 1.1 MΩ. Then C' = 34 pF and C'' = 39 pF. For the specimen thickness $d = 10^{-2}$ m and the angle = , it holds $B = 5.1 \times 10^{12}$ F^{-1}.m^{-1}.

4 CRACK FORMATION PROCESS

The sensor output voltage $u(t)$ depends on the time-dependent charge $q(t)$ and on the face displacement $x(t)$ from the original position, where $2x(t)$ is the crack width. The face movement velocity determines the face charge movement time rate. The crack formation process may be split into two phases. In the first stage, the crack unclenches and $q(t)$ and $x(t)$ are growing. In the second stage, which follows the crack unclenching, the charge may either be considered to be constant or falling exponentially in consequence of the material electrical conductivity, and the face velocity either zero or time variable. In this case, the faces can be considered to execute either periodical damped or aperiodically damped oscillations.

5 MODEL A

Let us assume the face charge and movement velocity to be constant. The solution of the differential equation (1) is of the form

$$u(t) = B q v \tau \left[1 - \mathrm{e}^{-\frac{t}{\tau}} \right], \tag{2}$$

where the integration constant K has been determined from the initial condition $u(0) = 0$. If the process first phase terminates at the time t_m, the sensor output voltage is $u(t_\mathrm{m}) = u_\mathrm{m}$ and the velocity $v = 0$. The solution then is

$$u(t) = u_\mathrm{m} \mathrm{e}^{-\frac{t - t_\mathrm{m}}{\tau}}. \tag{3}$$

The sensor output voltage versus time plot is shown in Fig. 2 (for t_m = 3 μs, $B = 5.1 \times 10^{12}$ F^{-1}.m^{-1}, τ = 37 μs, $qv = 10^{-10}$ C.m.s^{-1}, u_m = 1.48 mV).

As it holds

$$u_\mathrm{m} = B q v \tau \left[1 - \mathrm{e}^{-\frac{t_\mathrm{m}}{\tau}} \right], \tag{4}$$

the time t_m and the charge times velocity product qv can be determined.

In Fig. 3, experimental curves are best-fit-approximated by model A functions. On the basis of this approximation, parameters of this model can be subsequently determined.

In this way, following quantities have been found out: $\tau = 39.7$ μs, $Bqv\tau = 0.0374$ V, $u_m = 0.904$ mV, $t_m = 0.97$ μs (measured from the impulse starting point). From these data, the charge times face velocity product can be determined: $qv = 1.85 \times 10^{-9}$ C.m.s^{-1}.

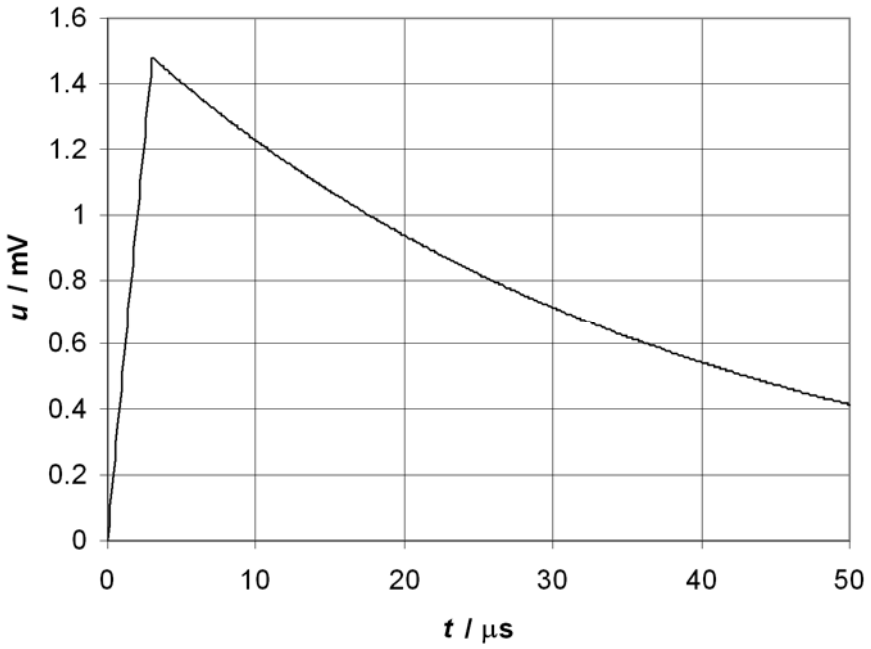

Figure 2: Theoretical sensor output voltage versus time plot, model A.

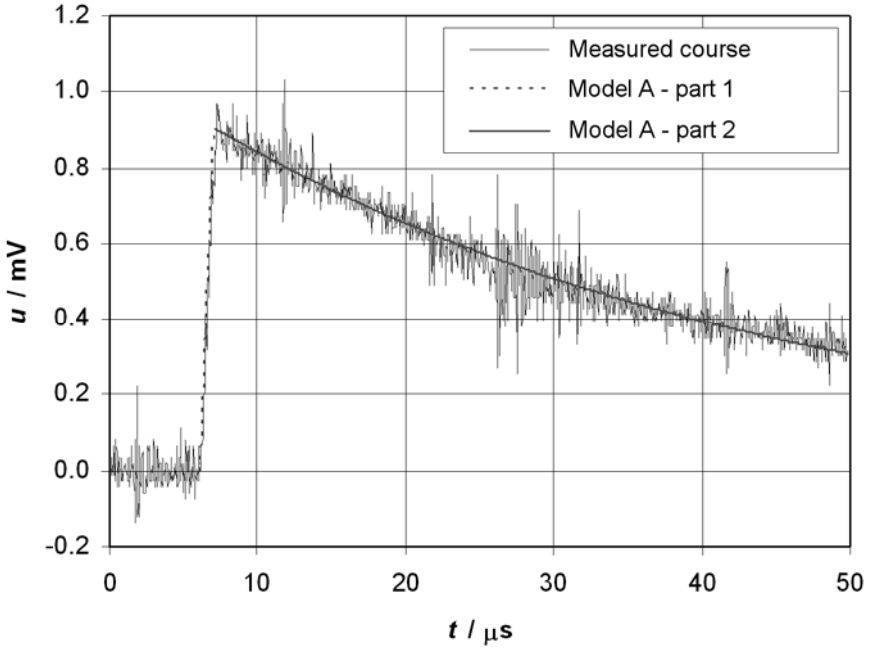

Figure 3: Comparison of experimental and theoretical time plots for model A, extren 68.028.

6 MODEL B

Let the charge $q(t)$ and the face displacement $x(t)$ from the equilibrium position be

$$q(t) = q_0 \left(1 - \mathrm{e}^{-\frac{t}{\tau_q}}\right), \tag{5}$$

$$x(t) = x_0 \left(1 - \mathrm{e}^{-\frac{t}{\tau_x}}\right), \tag{6}$$

where τ_q and τ_x are the time constants of the charge and face displacement. The crack face velocity then is

$$v(t) = \frac{x_0}{\tau_x} \mathrm{e}^{-\frac{t}{\tau_x}}. \tag{7}$$

Equation (1) has the following solution:

$$u(t) = \frac{B q_0 x_0}{\tau_x} \left(\frac{1}{D} \mathrm{e}^{-\frac{t}{\tau_x}} - \frac{1}{E} \mathrm{e}^{-\left(\frac{1}{\tau_q} + \frac{1}{\tau_x}\right)t} + \frac{F}{ED} \mathrm{e}^{-\frac{t}{\tau}} \right), \tag{8}$$

where $D = 1/\tau - 1/\tau_x$, $E = 1/\tau - 1/\tau_x - 1/\tau_q$, $F = 1/\tau_q$. The time plot of the quantity $u_0(t) = u(t)/(B\, q_0\, x_0)$ is shown in Fig. 4.

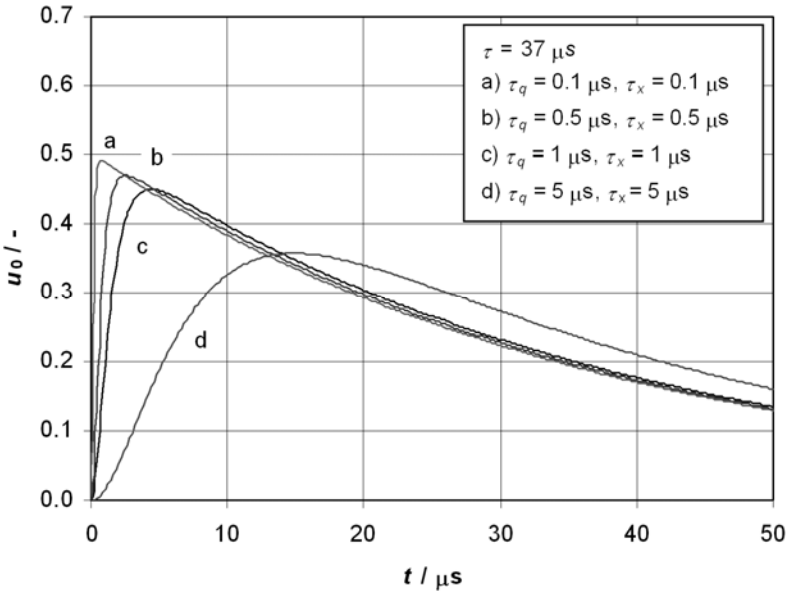

Figure 4: Theoretical time plot of the sensor normalized output voltage for model B and different time constants τ_q a τ_x.

In models A, B, it is assumed that the magnitudes of $q(t)$ and $x(t)$ do not change any more after they have reached their maximum values (in the second stage of the process).

In Fig. 5, the experimental curve is best-fit-approximated by function (8). From this plot, following quantities have been read out: τ_x = 4.66 μs, τ_q = 0.847 μs and τ = 12.1 μs. It is seen that the experimental curve fits the theoretical one very well (corresponding to (8)).

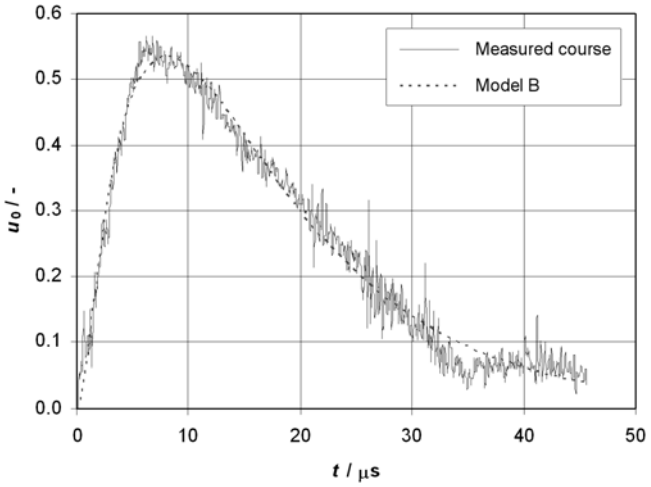

Figure 5: Comparison of experimental and theoretical time plots for model B, extren 61.097.

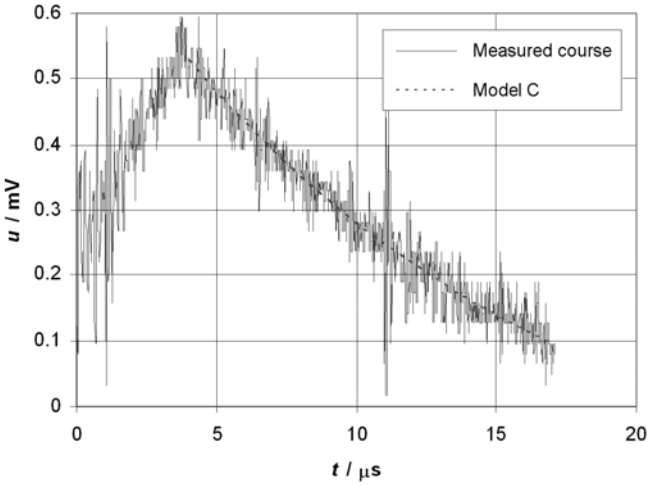

Figure 6: Comparison of experimental and theoretical time plots for model C, extren 58.050.

7 MODEL C

After the crack unclenches at time t_m, the face charge $q(t)$ and the face separation $x(t)$ either do not change (second stage of model A or B), or the crack faces execute damped oscillation and, possibly also, an electric charge relaxation takes place in consequence of the electric conductivity of the material which cannot be neglected. In the case of the face critically or supercritically damped oscillations, we may suppose

$$x(t) = x_m - x_0\,(1 - e^{-\delta(t - t_m)}), \tag{9}$$

$$q(t) = q_m\, e^{-\beta(t - t_m)}, \tag{10}$$

where x_m is the face displacement at time t_m, x_0 is the amplitude of the damped motion, δ is the mechanical damping coefficient, $1/\beta$ is the time constant of the electric charge relaxation.

Now, equation (1) has the following solution

$$u(t) = A\,\mathrm{e}^{-\gamma(t-t_m)} + (u_m - A)\,\mathrm{e}^{-\frac{t-t_m}{\tau}}, \quad t \geq t_m, \tag{11}$$

where $A = B\,x_0\,q_m\,\delta\,\tau/(\gamma\tau - 1)$ and $\gamma = \beta + \delta$.

The time plot of $u(t)$ is shown in Fig. 6 for $\tau = 37.0$ μs, $1/\gamma = 17.1$ μs, $A = 1.17$ mV, $u_m = 0.529$ mV.

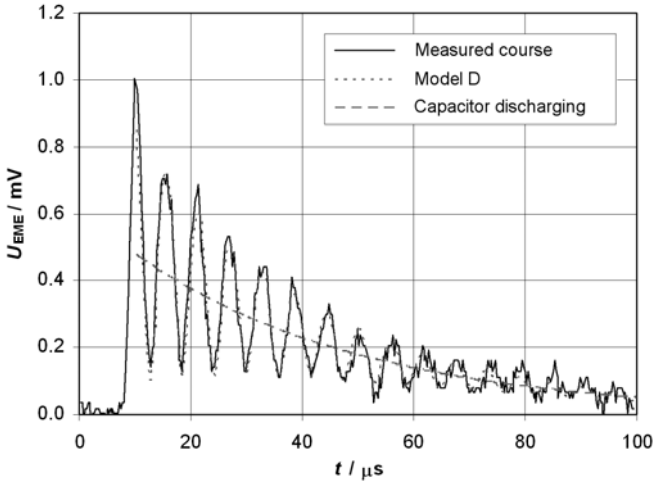

Figure 7: Comparison of experimental and theoretical time plots for model D, extren 52.023.

8 MODEL D

In the case of subcritically damped oscillations of the crack faces with angular frequency ω it holds

$$x(t) = x_m + x_0\,\mathrm{e}^{-\delta(t-t_m)}\sin\left[\omega\left(t - t_m\right) + \varphi_0\right], \tag{12}$$

where t_m is the time at which the crack face displacement x_m is maximum, δ is the mechanical damping coefficient.

In this case, equation (1) has the following solution

$$u(t) = U_0\mathrm{e}^{-\frac{t-t_m}{\tau}} - \frac{B\,b\,x_0 q_m\,\mathrm{e}^{-\gamma(t-t_m)}}{\sqrt{\omega^2 + \omega_0^2}}\sin\left[\omega\left(t - t_m\right) + \varphi_0 + \varphi + \psi\right], \tag{13}$$

where U_0 is an integration constant, $b = (\omega^2 + \delta^2)^{1/2}$, $\mathrm{tg}\,\varphi = -\omega/\delta$, $\gamma = \beta + \delta$, $\omega_0 = \gamma - 1/\tau$, $\mathrm{tg}\,\psi = \omega/\omega_0$, $1/\beta$ is the time constant of the electric charge relaxation.

The first term in (13) characterizes the discharging of a capacitor of a capacitance C' through a resistance R_1, the other term represents the response to the face charge oscillations.

Fig. 7 shows the experimental time plot of an EME voltage for extren 52.023 (the first curve). Following parameters have been determined for this plot and model D: ($U_0 = 4.77 \times 10^{-4}$ V, $\tau = 40.1$ μs, $B\,b\,x_0\,q_m / (\omega^2 + \omega_0^2)^{1/2} = 3.84 \times 10^{-4}$ V, $\gamma = 3.99 \times 10^4$ s^{-1}, $\omega = 1.09 \times 10^6$ s^{-1}, $\varphi_0 + \varphi + \psi = -1.38$). The second curve has been drawn using these quantities. The third curve represents the capacitor discharging transient.

9 CONCLUSIONS

Four models of EME signal generation in mechanically loaded composite materials have been put forward.

The simplest model, A, assumes the face charge and velocity to be constant. Although this is a heavy simplification, time plots corresponding to this model can be found in the signals being picked up.

Model B, which assumes both the charge and the crack face distance to follow an exponential law, appears very well suited for interpreting the measurement results.

Model C is well suited for the crack face damped oscillations after the crack unclenching.

Model D, which assumes quasi-harmonic oscillations of the crack faces after the crack unclenching, appears to be promising for the future from the viewpoint of the crack geometry studies. About 25 % of experimental time plots fall into this model type.

The above mentioned models can be applied to diagnosing mechanically loaded electrically non-conducting solids.

ACKNOWLEDGMENT

This paper has been prepared under the subsidy of the Research Intent No. MSM 0021630503, which is currently being dealt with at the Faculty of Electrical Engineering and Communication Technologies of Brno University of Technology.

REFERENCES

Koktavý, P.: 2009. *Experimental study of electromagnetic emission signals generated by crack generation in composite materials*. Meas. Sci. Technol, vol. *20, 015704*.

Chatiašvili, N. G.:1988. *Vozmožnye mechanizmy elektromagnitnovo izlučenija pri razrušeniji kristalov i gornych porod*. Geofizičeskij žurnal, vol. 10, pp. 45 – 53.

Chatiašvili, G.:1991. *Elektromagnitnoje izlučenije pri deformacii i razrušeniji gornych porod i kristalov*. AN Gruzii, Inst. geofiziki. "Mecniereba" Tbilisi.

Šikula, J., Koktavý, B., Vašina, P., Weber, Z., Kořenská, M., Lokajíček, T.:1996. *Electromagnetic and Acoustic Emission from Solids*. Proc. of 22nd European Conference on Acoustic Emission Testing, Aberdeen, UK.

Lokajíček, T., Šikula, J.:1996. *Acoustic Emission and Electromagnetic Effects in Rocks*. Progress in Acoustic Emission VIII, pp. 311 – 314.

Gershenzon, N., Gokhberg, M. Morgunov, V.: 1987. Sources of electromagnetic emissions preceding seismic events. Izv. Earth Phys, vol. 23, pp. 96 – 101.

The Problem of Testing the Grouting of Prestressing Reinforcement - Use of Radiography

O. Anton*
Brno University of Technology, Faculty of Civil Engineering, Brno, Czech Republic,
** Corresponding author: anton.o@fce.vutbr.cz*

DOI: 10.2478/v10158-010-0002-4

ABSTRACT: One of the less frequent requirements from real world condition is to verify the correctness of the grouting of prestressed reinforcement. The experiment described in this paper aims at examining the possibilities of Co-60 radiography in solving this problem, depending on the thickness of the concrete, the form of defect, and the space configuration of the radiography of this defect.

KEY WORDS: Radiography, prestressing cables.

1 INTRODUCTION

One of the tasks of standard practice is to verify the correctness of grouting of prestressing reinforcement. One of the few methods effective in this case is Co-60 radiography. The following experiment was supposed to examine the extent of the possibilities of this non-destructive method for various thicknesses of concrete and various forms of grouting defects. As this issue was only marginal in the extensive research in progress, the experiment was carried out for one shape alternative of prestressing reinforcement only.

2 SAMPLES AND CHOICE OF RADIOGRAPHIC CONFIGURATIONS

This experiment was carried out in connection with the previously performed tests related to the possibility of imaging and identification of steel reinforcement in concrete depending on the type of reinforcement, its diameter, depth of its placement, and on the thickness of irradiated concrete.

The Co-60 isotope placed in the TECH/OPS radiographic cover was used as the source of radiation. The Co-60 used for experiments had an activity of approx. 1TBq, and it is at the moment the highest activity isotope in the Czech Republic designated for the irradiation of structures.

On the basis of experience, we chose the most commonly used radiographic film with the D7 sensitivity, Testix C7 NEW NIF, which is probably the highest quality Agfa product. As regards the format, we chose the largest size available on the market at the moment, i.e. 400 x 300 mm. Solid film cassettes were equipped with a pair of lead intensifying foils, which made for a substantial shortening of exposures with a simultaneous minimum decrease in the quality of radiograms (the use of other than metal foils was

not considered, precisely for preserving the highest possible quality of radiograms). The films were developed using a standard development process in the darkroom of the Radiation Defectoscopy Centre. The use of new chemicals was guaranteed in order to lower the possibility of results deformation due to an incorrect development process.

The evaluation of radiograms was carried out on a pair of negatoscopes varying in the luminous intensity, which eliminated the possibility of misinterpreting the results due to the use of an unsuitable luminous intensity of the device. The apparatuses used were: L 120 apparatus with a lower luminous intensity but with a larger viewport, and Andrex with a higher, adjustable luminous intensity, but with a smaller viewport. For measuring the blackening of radiograms we used a densitometer with calibration scales for blackening.

We used an irradiation path made of concrete slabs with the dimensions of 500 x 400 x 50 mm in order to simulate various thicknesses of concrete. The path was complemented with samples in the form of concrete beams with the dimensions of 100 x 100 x 400 mm. In the centre of each beam, there was a plastic sleeve with a diameter of 50 mm. In the sleeve there was a prestressing cable made up of 7 wires with a diameter of 5 mm. The cable was then grouted in various ways and simulations of various grouting defects were made. The grouting was simulated by a compacted cement paste.

A total of five samples were created:

Sample 1 reinforcement fully grouted all along its length.
Sample 2 reinforcement grouted to a half of the length of the beam (duct).
Sample 3 reinforcement completely ungrouted all along its length.
Sample 4 reinforcement grouted longitudinally to a half of its length in the plane perpendicular (parallel) to the beam walls.
Sample 5 reinforcement grouted longitudinally to a half of its length in an inclined plane (grouting plane crosses the beam edges).

The last sample (beam labeled 0) was created as a comparative gauge with holes, where steel wires with diameters according to ČSN 73 13 76 were embedded in concrete transversely. This meant embedding two groups of wires in concrete, the first one, with diameters of 1, 2, 3, 4, 5, 6 mm, and the second one, with diameters of 4, 6, 8, 10, 14, 16, 20 mm. After the setting of the concrete, the wires were removed and the result was a sample with holes of precisely defined diameters.

Figure1: Sample 0 before removing the wires defining the future holes.

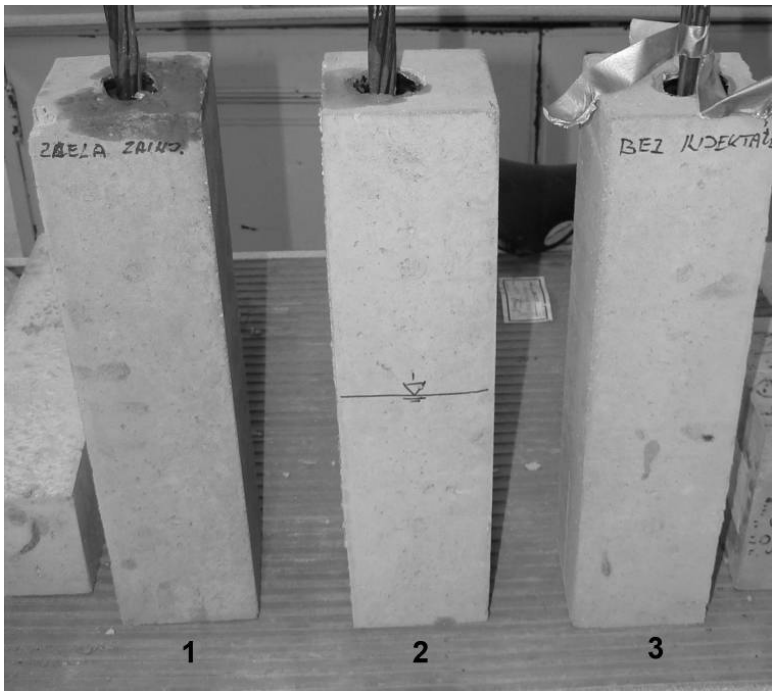

Figure2: Samples 1, 2 and 3 after the simulation of grouting.

Figure3: Sample 4 after the simulation of grouting, on the right we can see a part of sample 5.

Considering the experiment results, we could assume (in analogy with the reinforcement of the circular section) that the position of reinforcement in the profile will not be decisive; the decisive factor for the differentiability will be the thickness of concrete. That is why the radiographic configurations were simplified so that it could be possible, considering

the geometry, to always irradiate two samples at a time, i.e., samples were always placed as close as possible to the radiographic film.

Figure4: Irradiation path during the radiography of configuration A – 6.

The radiographic configurations were labeled with a transparent system of letters and numbers.

A – Samples 1 and 3 were irradiated
B – Samples 4 and 5 were irradiated
C – Samples 0 and 2 were irradiated

Number (1,2,3,4,5,6) – 1/100 of concrete thickness in mm

In order to avoid doubts in the identification of radiograms, during each exposure the surface of the outside slab was provided with a lead mark corresponding to the configuration mark.

3 FOCAL DISTANCE AND EXPOSURE TIME

In view of a suitable geometry of irradiation, the basic focal distance chosen was 400 mm. In the case of a greater thickness of concrete, the focal distance chosen equaled the thickness of concrete. With this focal distance we can still achieve acceptable exposure times. On the basis of the previous experiments, in places where radiation passed through the full concrete in all its thickness, the density of blackening chosen was about D = 3,0.

6 thicknesses of concrete were chosen for the experiment, from 100 to 600 mm (600 mm was taken as a boundary thickness for Co-60 irradiation).

Table 1: Proposed exposures and testing blackenings estimated.

Thickness of concrete (mm)	Focal distance (mm)	Exposure time (min)	Highest blackening estimated D
100	400	2.6	3.0
200	400	5.9	3.0
300	400	13.4	3.0
400	400	33.5	3.0
500	500	118.0	3.0
600	600	388.0	3.0

4 GAUGES AND DISCERNABILITY OF THE IMAGE OF HOLES

In the experiment we used an alternative gauge described above in the form of holes made in the beam. Positioning the gauge on the side of the irradiator, as described by the standard, was not possible due to the geometry of irradiation and high thickness of concrete.

It was found during the experiment that the group of holes with smaller diameters is, in fact, unusable; the group of holes with diameters 4 – 20 mm is sufficient.

An experiment was carried out to evaluate the discernibility of the radiogram according to ČSN 73 13 76 by the imaging of holes (a hole with the smallest diameter that is still visible is decisive).

Table 2: Evaluation of the discernibility of radiogram using the hole gauge according to ČSN 73 1376.

Thickness (mm)	Smallest diameter of the hole Dmin (gauge next to the film)	Discernibility of the radiogram Y (gauge next to the film)
100	3	3
200	6	3
300	8	2.7
400	14	3.5
500	16	3.2
600	20	3.3

In conclusion, it is possible to say that the discernibility of all images is in compliance with ČSN 73 13 76 as an approximate imaging method. As an exact method, however, none of the radiograms are satisfactory. Nevertheless, in this respect, the standard does not specify in more detail what both these types of methods represent in the identification of holes, and this classification is therefore largely irrelevant. Moreover, there is no need to point out that using similar gauges in practice for radiography in the field would be almost impracticable. Using the mentioned standard for this application of radiography is therefore absolutely impossible.

Much more interesting, however, is the possibility to identify holes of various sizes depending on the irradiated thickness, as seen in the following graph.

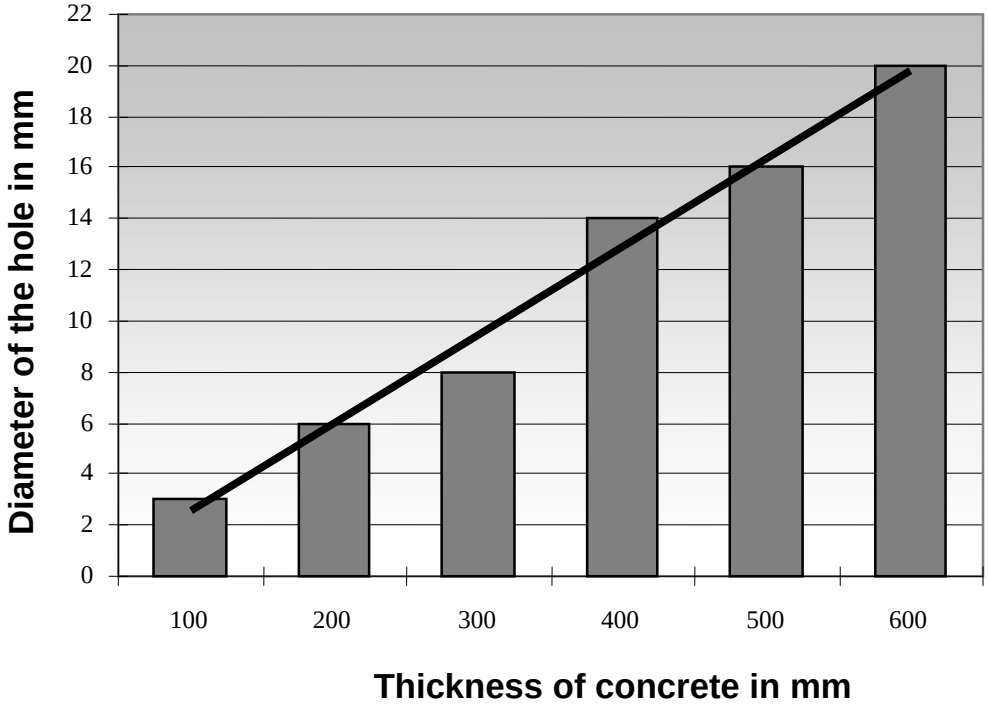

Figure5: Possibility to identify holes according to their size and thickness of concrete.

5 IDENTIFICATION OF PRESTRESSING REINFORCEMENT GROUTING DEFECTS

All the created samples were gradually irradiated in such a manner to simulate the total thicknesses of concrete from 100 to 600 mm. In all the radiograms, blackening was measured in the area of the grouted duct, the ungrouted duct, at the site of the displayed reinforcement, and immediately next to the duct.

All the radiograms, blackenings measured, and comments on radiograms can be found in Appendix 9.

5.1 Sample 1 – reinforcement fully grouted

Radiograms are characterized by an even blackening in the area of the sleeve of prestressing reinforcement. Blackenings at the site of the sleeve and outside it differ only very slightly (differences ranging from 0.01 to 0.04). It is possible to say that up to concrete thicknesses of 500 mm, the state can be evaluated as full grouting. In the case of greater thickness, this evaluation is doubtful.

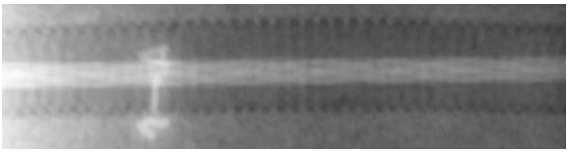

Figure 6: Sample 1, at a thickness of 100 mm, clearly visible homogeneity of grouting, blackening of the radiogram is even.

Figure 7: Sample 1, at a thickness of 600 mm, the picture is not really evaluable.

5.2 Sample 2 – reinforcement grouted to a half of the length of the beam

On the radiograms, there is a clearly visible characteristic divide between the grouted and the ungrouted part. Differences in the blackening between these parts range from 0.28 (for concrete thickness of 100 mm) to 0.12 (for 500 mm). Differences disappear only at a thickness of 600 mm, but also here the difference in the centre of the radiogram is apparent.

Figure 8: Sample 2, clearly visible difference on the divide between the grouted and the ungrouted part.

5.3 Sample 3 – reinforcement completely ungrouted

In the area of the sleeve, radiograms show a distinct blackening in comparison to the area outside the sleeve (at a thickness of 100 mm, the difference in blackening is 0.44, at 300 mm it is 0.21).

At a concrete thickness above 300 mm, it begins to be difficult to evaluate the edges of the radiogram, where the differences in blackening almost fade away.

At a concrete thickness above 500 mm, it is no longer possible to evaluate the radiogram without having a comparison of its grouted and ungrouted part attached to it.

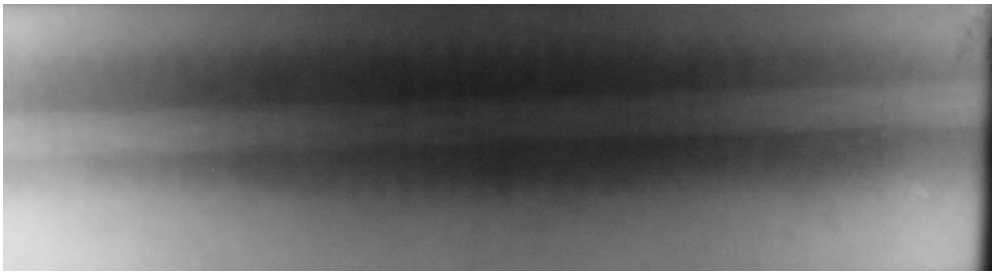

Figure 9: Sample 3, at a thickness of 400 mm, the marginal areas of the radiogram are not evaluable.

5.4 Sample 4 – reinforcement grouted to a half of the height of the beam (perpendicularly)

The evaluation of radiograms can be described as a combination of the previous cases. Due to great differences in the blackening of the grouted and ungrouted areas, it is possible to identify the grouting defect very well up to a concrete thickness of 600 mm. At thicknesses above 300 mm, it begins to be apparent that the blackening of the radiogram edges is lower and the evaluation of the marginal parts therefore more complicated.

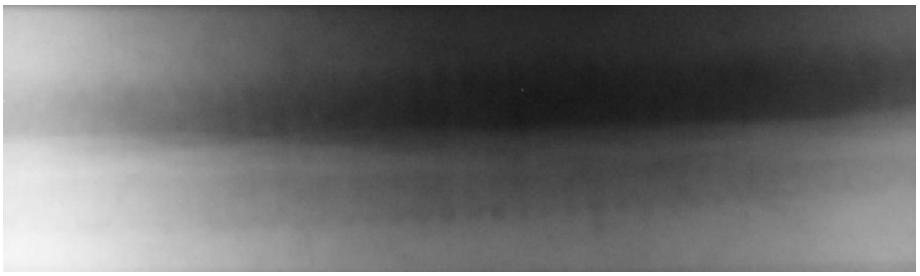

Figure10: Sample 4, at a thickness of 400 mm the marginal areas of the radiogram are not evaluable, but in the centre there is a clearly visible grouting defect.

5.5 Sample 5 – reinforcement grouted to a half of the height of the beam (diagonally)

The evaluation of radiograms can be described as a combination of the previous cases in samples 2 and 4. Differences in the blackening are not as distinct as in the previous cases, due to the overlapping of grouted and ungrouted areas (owing to the direction of radiation passage), nevertheless, it is possible to identify very well the ungrouted part of the profile up to a concrete thickness of 600 mm. At thicknesses above 300 mm, it again begins to be apparent that the blackening of the radiogram edges is lower and the evaluation of the marginal parts therefore more complicated.

6 IDENTIFICATION OF THE HOLES – CONCLUSIONS

It follows from the experiment that the possibility of hole identification evidently decreases proportionally to the thickness of the concrete, depending on the size of the hole. When Co-60 is used, the dependence between the thickness and the size of a hole of a circular section is given in Fig. 69.

Similarly, the possibility to evaluate the correctness of grouting of the prestressing reinforcement in the examined case depends, not only on the thickness of concrete, but also on the form of the grouting defect and the geometry of irradiation.

In the case of the method used, the thickness of concrete that can be regarded as reliable for the evaluation of radiograms and for determining the correctness of reinforcement grouting is 500 mm. Above this value, the evaluation is not accurate any more, except for the case when a radiogram captures the sharp transition between the grouted and ungrouted part.

At a thickness above 300 mm, the evaluation of the marginal parts of radiograms is not reliable any more, and if there was a defect there, it would be impossible to identify it. In the case of using radiography in situ it is therefore necessary to make several mutually overlapping exposures, so that the marginal area of one exposure is pictured in the centre of the neighbouring one. This will minimize the risk of non-detection of the defect.

REFERENCES

Anton, O.; Svoboda, D. The posibility of identification of the reinforcement in concrete using by radiographic checking with Co60. In Intrenational Topical Meeting VVER 2007. Praha, UJV. 2007. p. 1 - 6. ISBN 978-80-02-01980-0.

Anton, O.: Radiografická kontrola výztuže pomocí Co60 možnost přesného určení typu výztuže v závislosti na prozařované tloušťce. In Konference Zkoušení a jakost ve stavebnictví 2007. Praha, ČVUT v Praze. 2007. p. 145 - 150. ISBN 978-80-01-03794-2.

Non-linear Ultrasonic Spectroscopy as an Assessment Tool for the Structure Integrity of Concrete Specimens

M. Korenska* & M. Matysik
Department of Physics, Faculty of Civil Engineering, Brno University of Technology, Brno, Czech Republic
** Corresponding author: korenska.m@fce.vutbr.cz*

DOI: 10.2478/v10158-010-0003-3

ABSTRACT: On the basis of non-linear effect studies, new diagnostic and defectoscopic methods have been designed which are based on the elastic wave non-linear spectroscopy. The non-linear ultrasonic spectroscopy brings new prospects into the acoustic non-destructive testing of material degradation. Poor material homogeneity and, in some cases, the shape complexity of some units used in the building industry, are heavily restricting the applicability of "classical" ultrasonic methods. These linear acoustic methods focus on the energy of waves, which are reflected by structural defects, variations of the wave propagation velocity, or changes in the wave amplitude. However, none of these "linear" wave characteristics is as sensitive to the structure defects as the specimen non-linear response. In this way, non-linear methods thus open new horizons in non-destructive ultrasonic testing, providing undreamed-of sensitivities, application speeds, and easy interpretation. One of the fields in which a wide application range of non-linear acoustic spectroscopy methods can be expected is civil engineering. It is predicted that these advanced techniques can contribute a great deal to the improvement and refinement of the defectoscopic and testing methods in the building industry. The present paper deals with analyzing one of the non-linear ultrasonic defectoscopic methods from the viewpoint of its application to the concrete specimen structural integrity evaluation. Both intact specimens and specimens subject to various kinds of stress have been tested. The effect of structural defects on the elastic wave propagation has been studied.

KEY WORDS: Non destructive testing, nonlinear ultrasonic spectroscopy, concrete, structural integrity.

1 INTRODUCTION

Thanks to the turbulent development of concrete and reinforced concrete buildings taking place in the last century, the condition of concrete and reinforced concrete became a hot topic in the last decade. Concrete has proved to be a durable construction material in the past, however, concrete structures often experienced degradation after years of service. Rehabilitation techniques have been developed in foreign countries over several decades, showing a rapid development in general. However, the absence of an acceptable, relatively fast and cheap monitoring method, which would be capable of detecting structure faults at an early stage, and thus making a simple and cost-effective maintenance possible, is still persisting (Macecek, 2003).

On the basis of non-linear effect studies, new diagnostic and defectoscopic methods have been designed which are based on the elastic wave non-linear spectroscopy (Abeele and al. 2000, Johnson, 1999). Recently, various papers have been published on the theoretical or experimental verification of different methods in some application areas. One may state that it is still in its infancy, regarding the topic complexity, the requirements for newly developed special instrumentation and a high potential application diversity, the research and development of the respective methods, the required instrumentation and, last but not least, the practical applications of these methods,. On the other hand, most published papers, as well as our experience, show these methods to be highly promising for both defectoscopy and material testing purposes in the near future.

Our experimental and theoretical research work on Non-linear ultrasonic spectroscopy is focused on investigating non-linear ultrasonic transmission through building components from different inhomogeneous materials, such as ceramic, concrete, and reinforced concrete (Korenska & Manychova, 2008).

2 EXPERIMENTAL ARRANGEMENT

The method with one exciting harmonic ultrasonic signal was applied, where the generation of higher harmonics by a monochromatic excitation is evaluated. The experimental set-up and testing of its component units have been described in detail previously (Manychova, 2007) and will be only briefly described here, Fig. 1.

Figure 1: Experimental arrangement, photo of the non-linear ultrasonic equipment with a test specimen

The measuring apparatus consists of two principal parts, namely, a transmitting section and a receiving and measuring section. The transmitting section consists of four functional

blocks: a controlled-output-level harmonic signal generator, a low-distortion 100 W power amplifier, an output low-pass filter to suppress higher harmonic components and ensure the high purity of the exciting harmonic signal. The main chain of the receiving section includes an input amplifier with filters designed to minimize the receiving chain distortion and a band-pass filter amplifier. Having been amplified, the pickup output signal was then fed into a THPS3-25 HandyScope3 measuring instrument to be sampled and analyzed.

To interpret the recorded data properly, each of the measuring instruments must answer the demands of high linearity. For the purpose of improving the reliability and accuracy of the non-linear experiments and of minimizing the error effects the attention was focused on the transmission between transmitter and sensors. Elements meeting the given requirements were chosen (Korenska at al. 2006). A program package to control the measuring process, the data processing, and the evaluation makes for an indispensable tool. The measurement results were represented in the form of frequency spectra.

2.1 Intact Concrete Specimens

In the first stage of the experiment, we tried to find out whether the high inhomogeneity of the concrete material gives rise or does not give rise to the non-linear phenomena. Two groups of specimen were denoted A and B, both featuring the same concrete mix charge. Each group comprised of 10 specimens of dimensions 150 mm × 150 mm × 150 mm, the A group specimen having been aerated, whereas the B group ones were non-aerated.

2.1.1 Measurement Results

Fig. 2a) shows the results obtained from A-group specimens. It shows the frequency spectrum of the A3 specimen response to the harmonic ultrasonic excitation at a frequency of 29 kHz, as captured by a K33 sensor. The first five harmonic frequencies appear to be emphasized, their amplitudes decreasing with the serial number *n*. Similar results have been obtained from B-group specimens, as is seen in Fig. 2b), showing the frequency spectrum of the B4 specimen. A comparison of the diagrams shows that the aerated specimen of the A-group suppresses the higher harmonic frequencies more intensely, which is apparently due to the air pores in the specimen structure.

All of the specimens tested showed the same amplitude decreasing trend for the harmonic frequency increasing order.

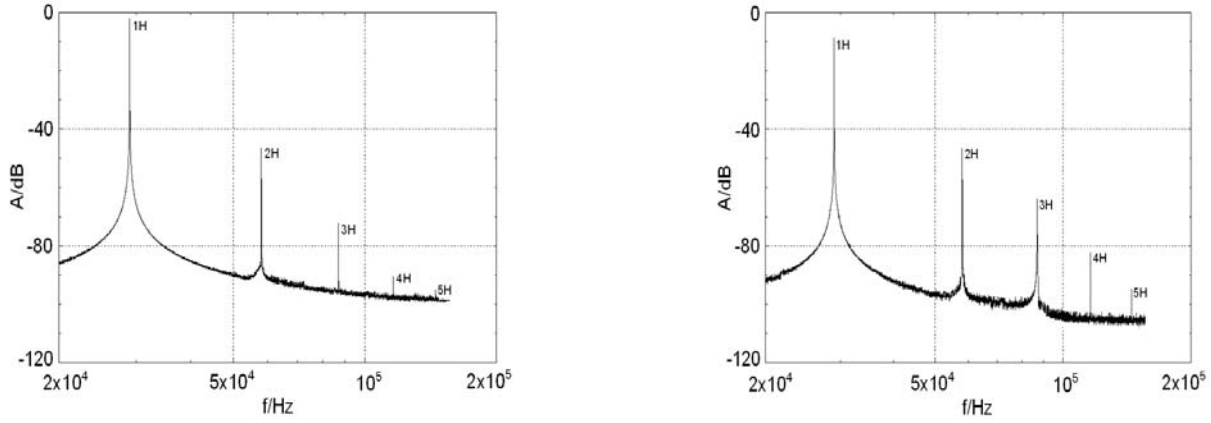

Figure 2: Frequency spectrum – a) A3 specimen, b) B4 specimen.

2.2 Freeze – Thaw Cycle Degraded Concrete Specimens

In the second stage, we studied the concrete specimen structure having been stressed by thermal shocks. The concrete specimens were stressed by recurrent freeze-thaw cycles. Measurements were realized after 25 and 50 freeze-thaw cycles.

2.2.1 Measurement Results

Figure 3 shows the high harmonics' amplitudes relative to the first harmonic's amplitude for the A2 specimen in all three conditions: pre-degradation (0 cycle), after 25 freeze-thaw cycles, and after 50 freeze-thaw cycles. The harmonic component amplitudes decrease with the serial number *n* increase in the case of pre-degradation condition. This is evidence of the fact that this inhomogeneous material creates no source of non-linear phenomena. The transfer characteristic, which corresponds to the same specimen having been subjected to 25 freeze-thaw cycles, does show a non-linearity. It becomes evident from a distinct drop of the fourth harmonic's amplitude (4H), which is exceeded by the fifth harmonic's amplitude (5H). Relative amplitude values corresponding to the specimen having undergone 50 freeze-thaw cycles also show non-linearities. In this case they consist of a drop of the third harmonic's amplitude and an increase of the fourth harmonic (4H).

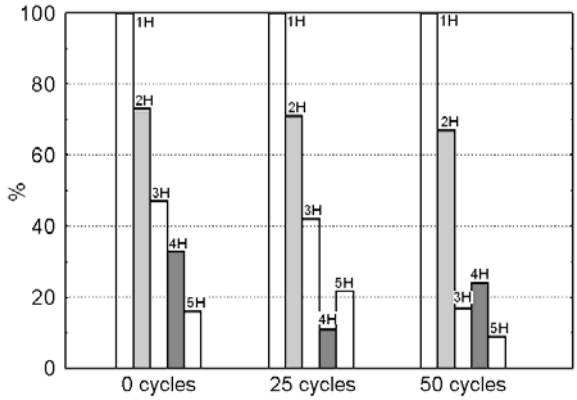

Figure 3: Relative amplitude values.

2.3 Polymer-Fibre-Filled Concrete Specimens

Finally, we tested concrete specimens of dimensions 100 mm x 100 mm x 400 mm which had been filled with polymer fibres. The specimens were examined for flexural tensile strength in a two-weigh pressing machine. The load test was terminated as soon as visible cracks appeared. These cracks closed again after the strain was removed. In the case of the TP7 specimen a visible crack remained after the specimen had been relieved. The transmitter and sensor configuration is shown in Fig. 4.

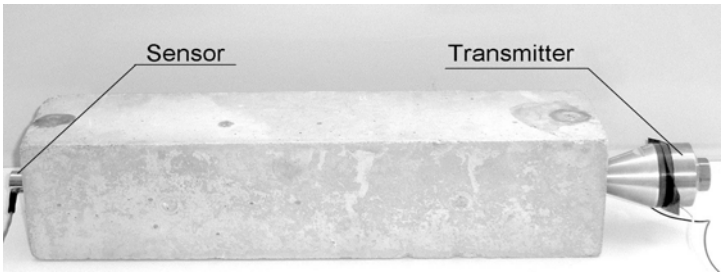

Figure 4: Location of the exciter and the sensor on the specimen under test.

2.3.1 Measurement Results

Pre-test measurements of the TP7 specimen are shown in Fig. 5. The shape of the frequency spectrum corresponds to that of the intact specimen and higher harmonic amplitudes are decreasing with their serial number.

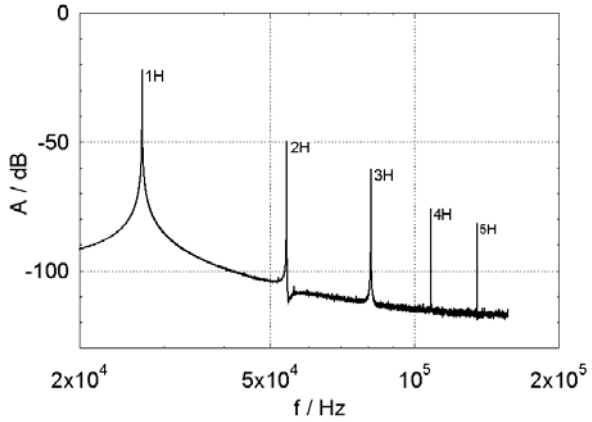

Figure 5: Pre-test frequency spectrum of TP7 specimen.

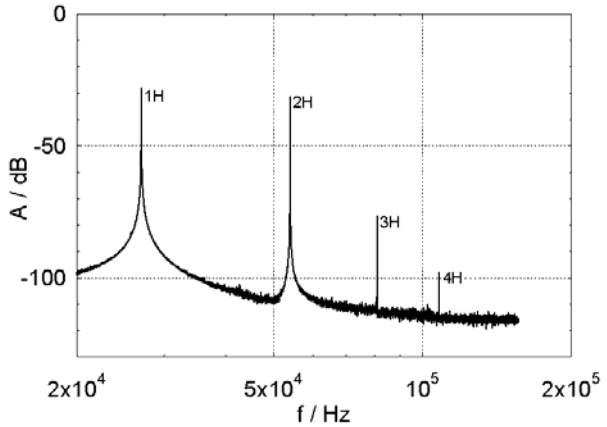

Figure 6: Frequency spectrum of TP7 after load test.

Fig. 6 shows the frequency spectrum of the same specimen after the load test was carried out in the pressing machine. When compared with Fig.5, the response function shows the higher harmonic frequencies to have lower amplitudes. The fifth harmonic has disappeared entirely which is probably due to the structure-degradation-induced higher attenuation. Another change consists of emphasizing the second harmonic's amplitude with respect to the first harmonic, as well as both the third and fourth harmonics.

3 CONCLUSION

This paper presents our first results of concrete specimen structure testing by means of non-linear ultrasonic spectroscopy using a single exciting harmonic frequency.

To properly interpret the measuring results, the transfer function of the whole measuring set-up must be determined and all measuring instruments must comply with high quality standards. It is therefore essential to minimize any harmonic distortion in the signal pick-up and amplification path by eliminating any spurious signals (*3* f_1 parasitic signal, noise) from the measuring apparatus stages. It should be noted that a perfect mechanical coupling must be ensured between the exciter and the specimen and, further, between the specimen and the pick-up element during the experiment setup process.

Our measurements show that the effect of a material inhomogeneity is very low in the case of non-linear ultrasonic spectroscopy, its non-linear effect being substantially lower than in the case of common defects.

Furthermore, it has been proved that structure defects, which are due to the freeze-thaw cycles as well as mechanical strain, have caused changes in the signal propagation frequency dependence function. Structural integrity deterioration has given rise to non-linear effects in the transfer functions, which correlated with the deterioration degree.

Verification measurements of fundamental physical quantities have also proved the structural degradation to be caused by specimen mechanical loading.

Acknowledgments

This research is supported by GA CR 103/09/1499 and MSM 0021630519 projects.

REFERENCES

Van Den Abeele, Johnson, P. A. and Sutin, A., 2000. *Nonlinear Elastic Wave Spectroscopy (NEWS) techniques to discern material damage. Part I: Nonlinear Wave Modulation Spectroscopy (NWMS),* Research on NonDestructive Evaluation 12, pp. 17-30.

Van Den Abeele, Carmeliet, J., James, A. Ten Cate, Johnson, P. A., 2000. *Nonlinear Elastic Wave Spectroscopy (NEWS) Techniques to Discern Material Damage. Part II: Single Mode Nonlinear Resonance Acoustic Spectroscopy.* Research on NonDestructive Evaluation 12, 31- 42.

Johnson, P. A., 1999. *The new wave in acoustic testing.* The J. Inst. Materials 7, 544-546.

Hajek, K., Sikula, J., 2005. *Testing of Low-Current Contacts Quality and Reliability by Using Third Harmonic Distortion.* IEEE Trans. on Components and Packaging Technologies 28, pp.717 – 720.

Korenska, M, Manychova, M., 2008. *Nonlinear Ultrasonic Spectroscopy Used to Detection of Ceramic Structure Damage.* Nonlinear Acoustics- Fundamentals and Applications, ISNA18, pp. 541-544, Ed. Bengt O. Enflo, Claes M. Hedberg, Leif Kari, American Institute of Physics, New York 2008.

Korenska, M., Pazdera, L., Matysik, M., 2006. *Testing of Pickups for Single-exciting-signal Non-linear Acoustic Spectroscopy.* International Workshop Physical and Material Engineering, Slovak University of Technology in Bratislava, pp. 70-75, Ed. Palackova, A.

Manychova, M. 2007. *Measuring Setup for the Nonlinear Ultrasonic Spectroscopy Method.* 37th International Conference Defektoskopie 2007, pp. 147-151, Ed. Korenska, M.

Převorovský, Z., Van Den Abeele, K.E. 2004. *Calibration Samples for Use in Nonlinear Ultrasonic Spectroscopy.* 34th International Conference and NDT Technique Exposition Defektoskopie 2004, pp. 347-349, Ed. Mazal, P.

Macecek, M., 2003. *Ultrasonic Concrete Testing.* 33rd International Conference Defektoskopie 2003, p. 117-132, Ed. Mazal, P.

Optimizing the Location of Piezoelectric Sensors

I. Plšková* & Z. Chobola & M. Matysík
Department of Physics, Faculty of Civil Engineering, Brno University of Technology, Brno, Czech Republic
** Corresponding author: plskova.i@fce.vutbr.cz*

DOI: 10.2478/v10158-010-0004-2

ABSTRACT: Piezoelectric sensors appear to be best suited for picking up acoustic signals thanks to their high sensitivity over a wide frequency range, frequency response stability, design compactness, and reliability. Their design differs from sensor to sensor, depending on the type of the measurement to be carried out. Piezoelectric sensors are manufactured on the basis of crystals and polarized dielectrics. They feature, above all, a very good signal-to-noise ratio, a fast response to the load change and a wide range of operating temperatures. Along with the measurements of the noise voltage spectral density, the sensor sensitivity measurements are of high importance not only for the development of acoustic methods but also for the sensor application and, above all, checkout. The present paper deals with our test results of piezoelectric sensors from the following viewpoints: frequency range, response uniformity, sensitivity, and optimum location of a selected sensor with regard to the amplitude of the response signal from a ceramic tile.

KEY WORDS: piezoelectric sensor, ceramic tile, Impact-echo method.

1 INTRODUCTION

An ideal sensor should be compact, highly sensitive, easy-to-attach to the specimen, low-cost, and of simple design. Furthermore, it should feature a high sensitivity throughout the whole frequency range and a linear response curve. The main requirements concerning the sensor material are: high piezoelectric sensitivity, good mechanical rigidity, and permittivity. Piezoelectric sensors are manufactured on the basis of crystals and polarized dielectrics. The output signal is an electric charge. The design of a piezoelectric sensor is based on the piezoelectric effect which consists of the following: due to a mechanical deformation, electric polarization takes place inside some polycrystalline dielectrics. Image charges subsequently arise on their surface, being able to bind or release real charges on the attached electrodes.

As soon as the voltage vanishes, the dielectric returns to its initial state. Acoustic emission sensors transform acoustic emission wave packets into electric signals. An analysis and visualization of the signal is usually carried out after the measurement is finished, i.e., when the registration cycles of one or several concurrent impulses are completed. If the sensor system detects several acoustic emission packets during a predefined time interval, we can – under certain circumstances – assume the impulses to have been produced from a single acoustic emission source (i.e., they are supposed to have the same cause). The emission source can be located by means of two methods in specimens where the lengthwise dimension prevails. In the case of the so-called "point" location, the time differences between the acoustic emission impulse arrival times to different sensors are used to calculate

the coordinates of the acoustic emission source. If the "zone" location is used, only the sequence in which the acoustic emission impulses arrive at the different sensors is used. An advantage of the "zone" location consists of the fact that the information is sufficient even if the impulses are detected by only a single sensor. In the "zone" location method, each acoustic emission signal source is assigned to a "primary zone", which is determined by the sensor which has been the first to detect the acoustic emission packet.

The sensor output signals are amplified, filtered and saved. The data registration process will start when the magnitude of the amplified and filtered signal exceeds the predefined threshold level. The measurement of an acoustic emission wave packet will be terminated if the measured signal amplitude fails to exceed the predefined threshold level during a preselected time interval.

In the case of acoustic emission, propagating surface tension waves and vibrations, mostly in the frequency range from 20 kHz to 2 MHz, are picked up. There are certain types of tasks which require another frequency range. For example, when tracking phase transformation processes, frequencies of the order of MHz are picked up. The sensor design is therefore different, depending on its intended application. The sensor types most frequently used are as follows: piezoelectric, capacitance, electromagnetic, strain-gauge, mechanical, laser and others.

2 EXPERIMENT

2.1 Piezoelectric sensor frequency characteristics

Piezoelectric sensors were tested in cooperation with the Department of Physics of the Faculty of Electrical Engineering and Communication Technologies. The objective of the tests consisted of selecting the best suited sensors from the viewpoint of frequency range, sensitivity, and response uniformity. Sensors made by the following manufacturers were tested: Vibra Metrics, Physical Acoustic Corporation and Sedlak. The noise characteristic (noise voltage spectral density versus frequency plot) measuring apparatus comprises of the acoustic emission sensor under investigation, a preamplifier, an amplifier, an oscilloscope intended to measure the rms value of the amplified signal, and, finally, a PC, intended to record and further process the data measured. Figures 1 through 6 show the noise frequency characteristics of PICO 1, PICO 2, Sedlak 7, Sedlak 10, Vibra Metrics 501, Vibra Metrics 516 sensors.

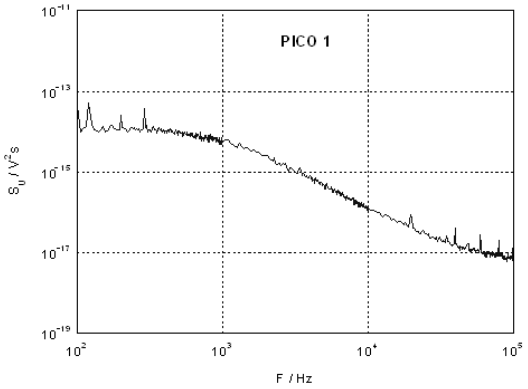

Figure 1: The noise frequency characteristics of sensor PICO 1.

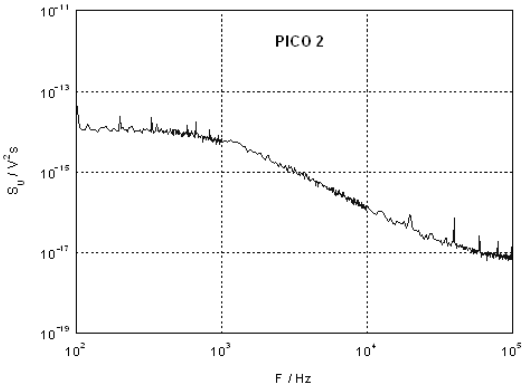

Figure 2: The noise frequency characteristics of sensor PICO 2.

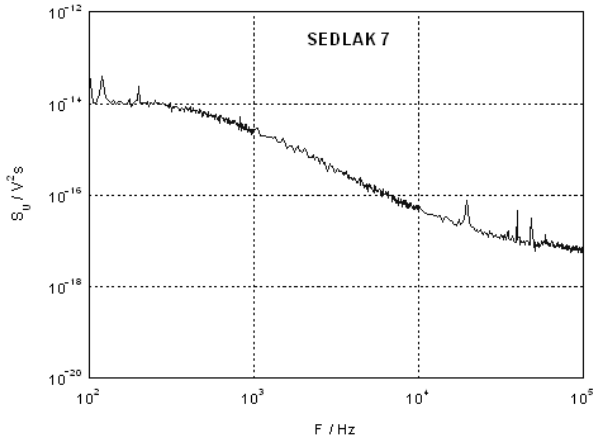

Figure 3: The noise frequency characteristics of sensor SEDLAK 7.

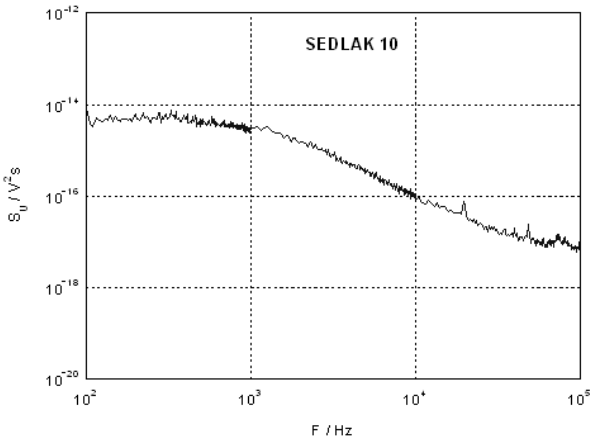

Figure 4: The noise frequency characteristics of sensor SEDLAK 10.

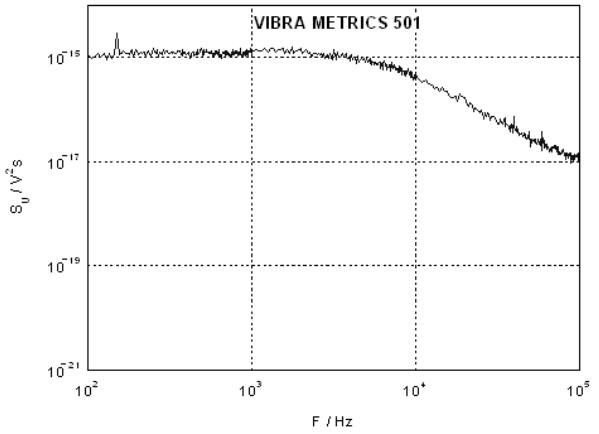

Figure 5: The noise frequency characteristics of sensor VIBRA METRICS 501.

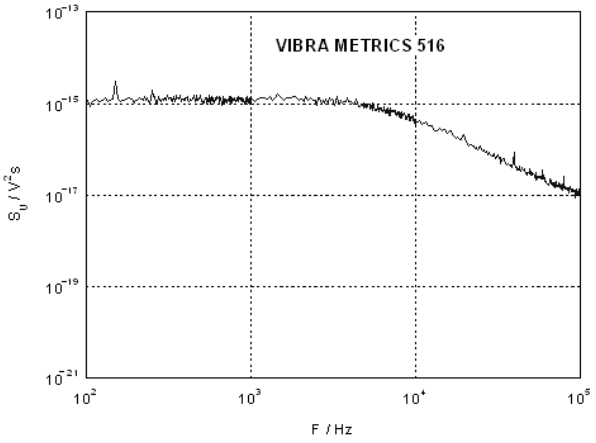

Figure 6: The noise frequency characteristics of sensor VIBRA METRICS 516.

2.2 Signal amplitude versus sensor position

To find the optimum sensor position, we studied experimentally the distribution of the read-out signal amplitudes throughout the tile surface. This study's results provide information on the best position of the sensor in the tile surface for subsequent experiments. A single specimen of dimensions 30 x 30 cm has been selected from the batch of intact ceramic tiles. A line grid was drawn in the surface of the ceramic tile, see Fig. 8. Sedlak type sensors were placed sequentially at different specimen surface grid points. Fig. 7 shows in detail how a Sedlak type piezoelectric sensor is fastened to the ceramic tile surface. Bees wax served as interface between the sensor and the specimen. The measuring point spacing was 1.5 cm. The tile side edge measuring point spacing was 1.5 cm, too.

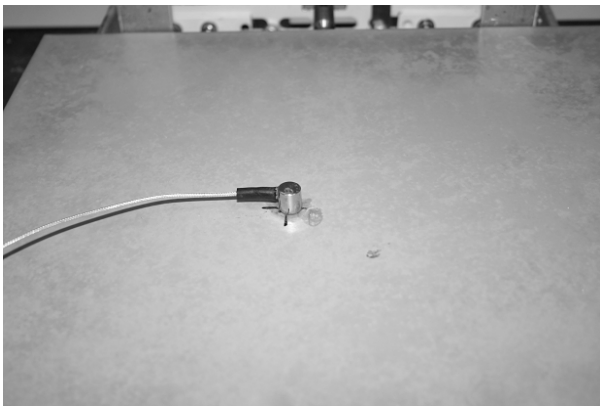

Figure 7: Detailed view of the sensor (SEDLAK) fastening method to the ceramic tile surface.

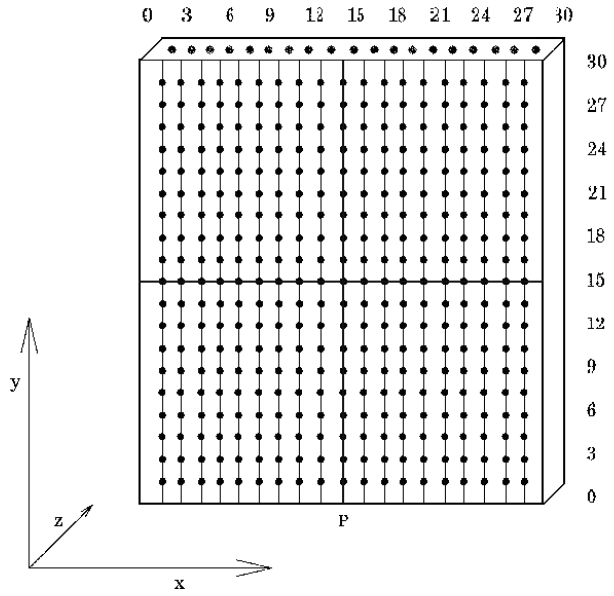

Figure 8: Measuring point distribution over the ceramic tile surface.

The exciting impulse was generated by means of a hammer blow, acting from a constant height and at a defined point of application, for the sake of ensuring identical experiment conditions. The impulse application point P was selected to be in the middle of the specimen side edge. Piezoelectric sensors, attached to the tile surface at designated points, were used to pick up the tile response to the exciting impulse. A digital oscilloscope was used to record and visualize the response voltage, which was further processed by means of special software.

The distribution of the response signal amplitudes over the tile surface is shown in the diagram of Fig. 9. Figure 10 shows the waveform as determined from the response signal amplitude being picked up at the tile side edge.

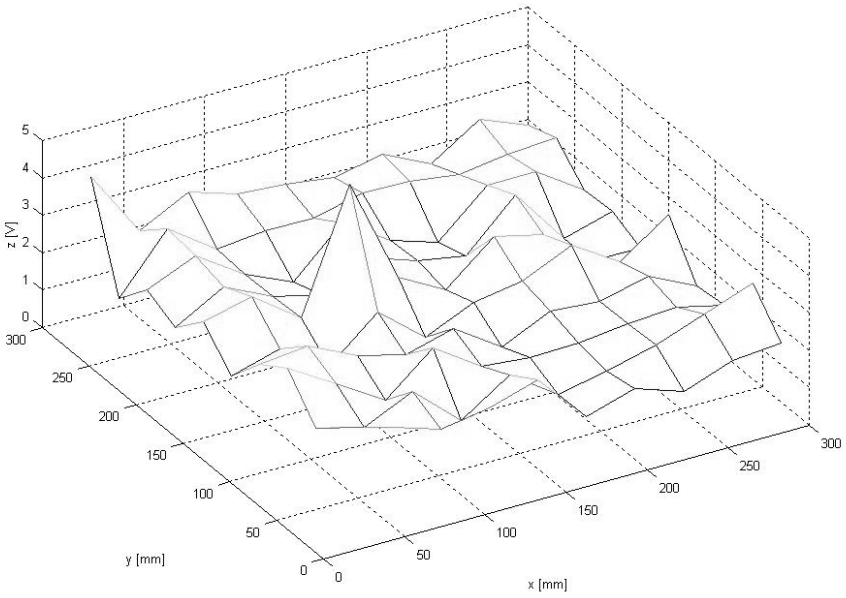

Figure 9: Distribution of amplitudes over the ceramic tile surface.

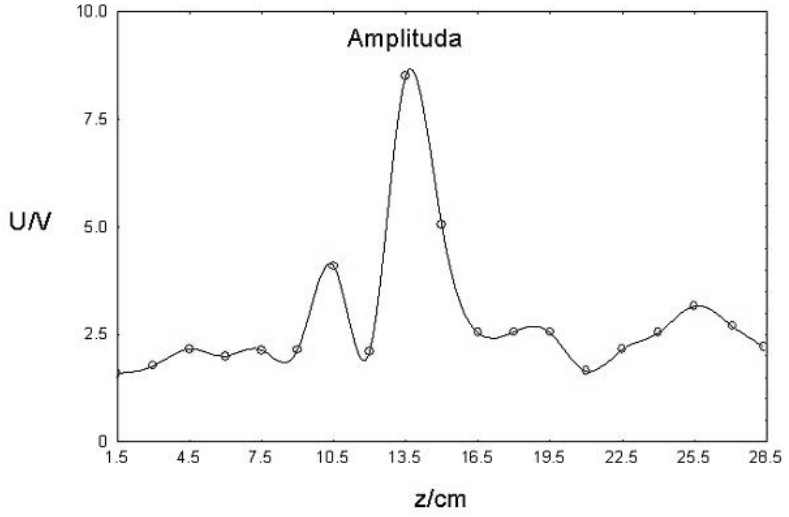

Figure 10: Waveform of a flexure wave at the ceramic tile side edge.

3 SUMMARY AND CONCLUSIONS

Following conclusions can be derived from our results:

- Based on our tests of piezoelectric sensors manufactured by Vibra Metrics, Physical Acoustic Corporation and Sedlak, we have selected Sedlak type piezoelectric sensors as the best suited ones, thanks particularly to their high sensitivity and a flat frequency response in the range from 100 Hz to 50 kHz.

- An experimental study of the acoustic emission signal distribution was carried out in order to find the optimum sensor position in the ceramic tile surface and side edge. Based on this study, information about the optimum sensor position was gained. To reach the highest sensitivity, the sensor was placed at a point of coordinates x = 12 cm, y = 18 cm, and, for side edge sensing, at z = 13,5 cm, in both cases on the surface of a tile of dimensions 30 x 30 cm. Identical measurements were also carried out on ceramic tiles of dimensions 33 x 33 cm. The best sensor position was x = 18 cm, y = 16.5 cm for tile surface pick-up and z = 16.5 cm for tile side edge pick-up.

- The above mentioned results are going to be used to determine the sensor positions in ceramic tile frost resistance testing experiments.

ACKNOWLEDGEMENTS

This research has been supported by the Ministry of Education of the Czech Republic, under contract MSM0021630519 and by project of GACR No.103/09/P247.

REFERENCES

Plšková, I.: 2006. *Využití frekvenční inspekce pro posouzení mrazuvzdornosti keramické dlažby:* disertační práce. Brno: Vysoké učení technické v Brně, Fakulta stavební, 2006. 117 s.

Serridge M., Licht T.R., 1987. *Piezoelectric Accelerometer and Vibration Preamplifier Theory and Application Handbook*, Denmark, 1987.

Kazakov V.,P. A. Johnson P. A., 2002. *Modulation Acoustic Method of Crack Location.* 16th International Symposium on Nonlinear Acoustics Moscow, Russia August 2002.

Majzner J., 2003. *Citlivost a šum piezoelektrických snímačů akustické emise*, In Proc. Of the Workshop NDT CMC 2003 Non-Destructive Testing of Civil Engineering Structures and Constructions, Czech Republic, ed. by Technical University of Brno, 2003,ISBN 80-7204-318-8.

Yong-Dong Li, Kang Yong Lee, 2009. *Fracture analysis on the arc-shaped interface in a layered cylindrical piezoelectric sensor polarized along its axis.* Engineering Fracture Mechanics, Volume 76, Issue 13, September 2009, Pages 2065-2073, ISSN 00137944.

Fast Impedance Spectroscopy Method for Insulating Layers with Very High Impedance

P. Schauer *
Department of Physics, Faculty of Civil Engineering, BUT, Zizkova 17, 602 00 Brno, Czech Republic
** corresponding author: schauer@dp.fce.vutbr.cz*

DOI: 10.2478/v10158-010-0005-1

ABSTRACT: This paper presents the fast impedance spectroscopy method for objects with a very high impedance $|Z_x| \geq 1G\Omega$ modeled by RC networks. The method is suitable for predicting the lifetime and reliability of insulating materials. The fast impedance spectroscopy method was tested on insulating layers which were part of the system metal-insulator-metal (MIM). The method is based on measurements of the power loss and phase shift in the AC voltage divider, which consists of the measured system MIM and of the known impedance. Computer controlled instruments measure the gain and phase shift between the two outputs of alternating electrical circuit and a computer program calculates the parameters of the impedance spectroscopy from these values. The output is the graphical and tabular impedance characteristics of the MIM system, namely: the dielectric loss of the insulating film, imaginary part of impedance, loss factor, parallel resistance R_p and the capacity C_p of the MIM system, all frequency dependent. Frequency characteristics provide an analysis of loss mechanisms that may affect the quality and reliability of the insulating layers.

KEY WORDS: computer program, impedance spectroscopy, loss factor, insulating layers.

1 INTRODUCTION

Insulators and dielectrics have an irreplaceable role in electrical engineering and their presence is a necessary condition for the function of almost every electrical device. High-voltage electrical insulators are of special importance, where their quality affects the life and reliability of the whole equipment. The quality of the insulation material is limited by the working electric field intensity. Insulators are used in insulated wires and cables, in electrical machines and devices, and transformers and electric motors. High-voltage electrical engineering uses capacitors, as well as printed circuit boards. The most important material characteristics of insulators are conductivity, permittivity, dielectric loss factor and electrical strength. In most technical applications the dielectric losses are a scourge, causing dielectric heating and subsequent deterioration of its functional characteristics and reliability, especially in power applications.

Most recently a new method of dynamic monitoring of insulators and dielectrics was developed, known as impedance spectroscopy. It monitors the complex impedance dependence on frequency. The important dependences of impedance spectroscopy are mainly:

the frequency dependence of the real part of impedance, the frequency dependence of resistance, and, mainly, the frequency dependence of loss-factor, which is independent of the geometry of an insulator, which is a parameter of material only.

2 THEORY

From a physical point of view we can distinguish three main processes that give rise to dielectric losses:

1. The main process causing the dielectric loss is the process of electrical conductivity. This type of the dielectric loss is called **conductivity losses**. Conductivity losses appear in all types of dielectrics and insulators. Most apply at higher temperatures.

2. The second dielectric losses are **polarization losses**. These losses are usually only found in a certain temperature range where the loss polarization applies. They are already noticeable at less than microwave frequencies.

3. Ionization losses are added to the above processes in strong electric fields. Ionization losses exist because of dielectric ionization.

The processes of conductivity losses, polarization losses, and ionization losses are independent in the analysis of dielectric losses and thus, according to the additive principle, they are the sum of the individual components.

Dielectric losses are defined by the power relationship

$$P = UI\cos\varphi . \qquad (1)$$

Here U, I are the voltage RMS and current RMS respectively, φ is the phase shift between current and voltage. It is not convenient to express dielectric loss directly because it depends on the geometry of the material. It is better to introduce a loss factor, which is a material parameter, independent of geometry. The dielectric losses are described by the relationship

$$\tan\delta = \frac{P}{U^2\omega C} . \qquad (2)$$

C is the capacity and ω is the frequency. In non-polar dielectrics, the conductivity losses only occur depending on the frequency of the electric field, at $P = const$. Consequently, according to equation (2), loss factor must be hyperbolic with increasing frequency, $\tan\delta \sim 1/f$. Model behavior is shown in Figure 1, in logarithmic scales, for three different values of P/U^2 and for the value of capacity C = 50 pF.

As Figure 1 shows, the conductivity loss component of the loss-factor added to the polarization component in polar dielectrics. As such, the polarization component of the loss-factor reaches a peak when the reverse frequency value equals the time constant of the relaxation polarization effect $\omega = 1/\tau$. The loss-factor has a similar dependence as a resonance curve.

Curve 4 in Figure 1 is modeled by the equation

$$\tan\delta = \frac{a}{\sqrt{b^2 + (c\omega - \frac{1}{d\omega})^2}} \quad , \qquad (3)$$

where constants *c*, *d* satisfy the condition of frequency maximum of polarization loss-factor

$$\omega_m = \frac{1}{\sqrt{cd}} \quad . \qquad (4)$$

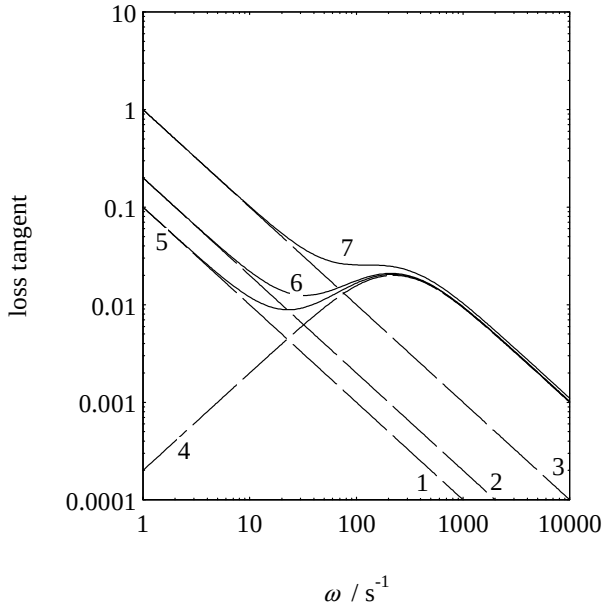

Figure 1: Model of the loss-factor dependences versus electric field frequency, both in logarithmic scales. Dashed curves 1, 2, 3 of type 1/*f* correspond to conductivity losses. Conductivity loss-factor is modeled according to equation (2) for three different values of P/U^2 and for the value of capacity *C* = 50 pF. Dashed curve numbered 4 (with a maximum) corresponds to polarization losses. Full curves 5, 6, 7 are the sum of both components.

The total loss factor is the sum of the above mentioned two loss mechanisms. Local excess of the curve $\tan\delta = f(\omega)$ over the hyperbole indicates the presence of dielectric polarization, which is a negative indicator for the reliability and quality.

Another view of the loss mechanisms can be seen if we plot dielectric losses *P*, depending on the frequency, for the same model parameters as in Figure 1. The results are shown in Figure 2. Curves are obtained by multiplying the loss-factor by $U^2\omega C$, see equation (2). Numbering of curves in Figure 2 corresponds to numbering in Figure 1. We see that while the conductivity losses component (curves 1, 2, 3) is frequency independent and applies even at low frequencies, polarization losses (curve 4) do not apply for the low frequencies, because it is very small. However from a certain frequency, when sharply increasing,

polarization losses apply, and for sufficiently high frequency polarization losses are, like conductivity losses, constant.

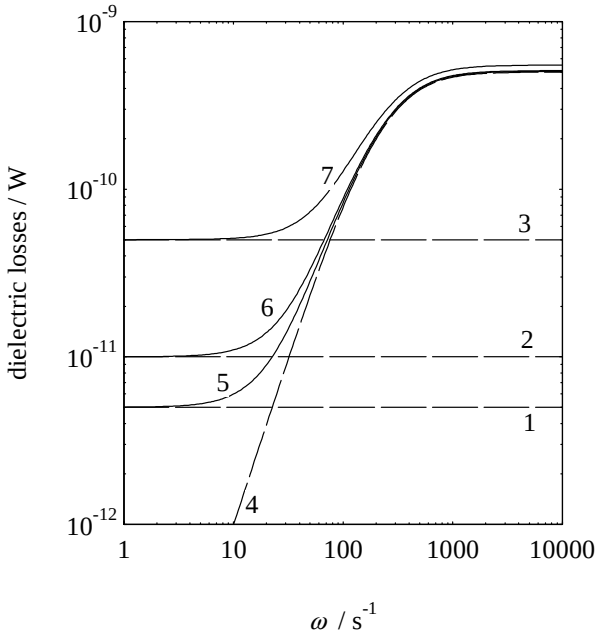

Figure 2: Dielectric losses versus frequency for the same model parameters as in Figure 1. We multiplied the loss-factor by $U^2\omega C$ value using equation (2), where $U^2C = 50 .10^{-12}$ J. Numbering of curves corresponds to those in Figure 1.

While polar dielectrics have a much higher relative permittivity compared to the non-polar, its value depends on the temperature and electric field frequency. Thus they have a much higher frequency-dependent dielectric loss and much higher conductivity than the non-polar, which also depends on temperature. Humidity has a considerable effect. With the exception of lower temperatures, polar dielectrics have significantly less electrical resistance than un-polar. All these features indicate that the study of the presence of the polarization phenomena in dielectrics is important diagnostic information about the quality and reliability of a dielectric insulator.

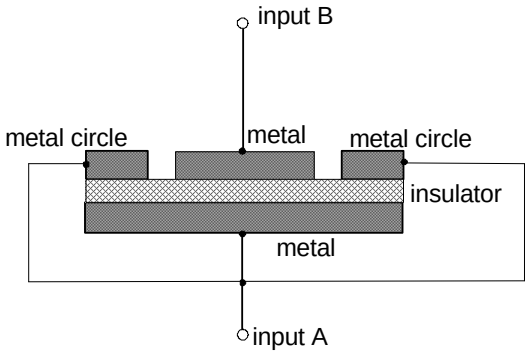

Figure 3: Insulating film is placed in a metal holder.

EXPERIMENTAL SETUP

The detailed setup of the MIM system is shown in Figure 3. A metal holder consists of a bottom circular electrode attached to the input A of the gain-phase meter (Figure 4) and opposite top circular electrode is connected to input B of the gain-phase meter. The ring around the top metal electrode is electrically connected with the bottom electrode. The holder was made of brass.

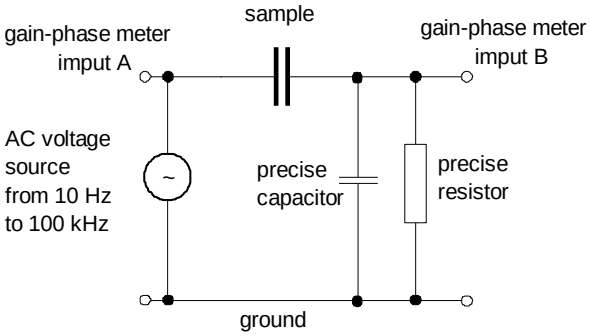

Figure 4: Detailed schema of blocks AC VS and DUT from the Figure 5. Exact resistance 1.07 MΩ consists of input B resistance, capacitor consists of B input capacity 112 pF.

Frequency dependences of physical quantities evaluated in the impedance spectroscopy were detected from the ratio of voltage and the phase shift of inputs A, B of the gain-phase meter (Figure 4). We used the instrument Hewlett Packard HP3575A, which operates in the frequency from 1 Hz to 13 MHz. The circuit was fed with a signal generator connected to input A.

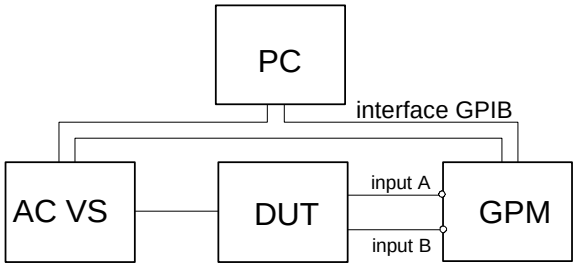

Figure 5: Block diagram of the measuring arrangement. AC VS is alternating sinusoidal current supply, DUT is MIM device under test, the GPM is gain phase meter and the PC is the computer.

Figure 5 shows the block diagram of the setup, where AC VS is the sinusoidal signal generator working in the frequency range from 1 Hz to 13 MHz, DUT is tested MIM system (device under test), the GPM is the gain phase meter with two inputs and the PC is the computer.

Gain L and phase shift φ between the inputs A, B were measured. Gain is defined as

$$L = 20\log K \quad , \qquad (5)$$

where $K = U_B / U_A$. It seems that the equivalent parallel RC circuit corresponds best to the MIM systems in real conditions. Therefore we replaced the tested MIM system with a RC combination $R_p = R_x$ and $C_p = C_x$. Under these conditions, the phase of the parallel impedance of resistance R_B and input capacitor C_B (of GP meter) is

$$\varphi_B = -\arctan \omega R_B C_B \quad , \qquad (6)$$

Impedance of parallel combination of R_B, C_B can be calculated as

$$Z_x = \frac{Z_B \sin\varphi}{K - \sin(\varphi_B - \varphi_x)}, \qquad (7)$$

Phase of Z_x is

$$\varphi_x = \varphi_B + \arctan\frac{\sin\varphi}{K - \cos\varphi}. \qquad (8)$$

Measured impedance Z_x will have a value

$$Z_x = \frac{Z_B \sin\varphi}{K - \sin(\varphi_B - \varphi_x)} \quad . \qquad (9)$$

Its real part is

$$\mathrm{Re}(Z_x) = Z_x \cos\varphi_x \qquad (10)$$

and its imaginary part is

$$\mathrm{Im}(Z_x) = Z_x \sin\varphi_x \quad . \qquad (11)$$

Hence loss factor of the test insulator, defined by the ratio of imaginary and real part of impedance Z_x is

$$\tan\delta_x = \frac{1}{\tan\varphi_x}, \qquad (12)$$

the resistance of the parallel RC circuit of MIM system is

$$R_x = \mathrm{Re}(Z_x)(1 + \tan^2\varphi_x) \qquad (13)$$

and its capacity is

$$C_x = -\frac{\tan \varphi_x}{\omega R_x}. \qquad (14)$$

3 COMPUTER PROGRAM

Our measuring program measures the mentioned parameters of the impedance spectroscopy using a computer with the GPIB bus and evaluates impedance characteristics of the height ohms samples, in accordance with equations (5) to (14). Program IMPEDANC was written in the language Turbo Pascal (Borland) for OS DOS. It applies object oriented programming for easy and efficient use. It is in the windows architecture, and steps are offered through the menu. The operator can use the mouse.

3.1 Program description

The main menu of the program IMPEDANC is in Figure 6. The menu allows choosing the main operations, such as head, measurement, numerical processing of the results and graphical processing of results. It is possible to return to any step whenever operator wants. The program has help that can be called either from the main menu or at any time during the measurement by pressing the F1 key.

Figure 6: The main menu of the program impedanc.exe.

3.1.1 Header creation

Before we start the measurement we create a header from the main menu. Menu environment is shown in Figure 7. The header is pre-defined in the file IMPEDANC.INI. Item measure name may not remain empty, otherwise the completion of the header will be not allowed.

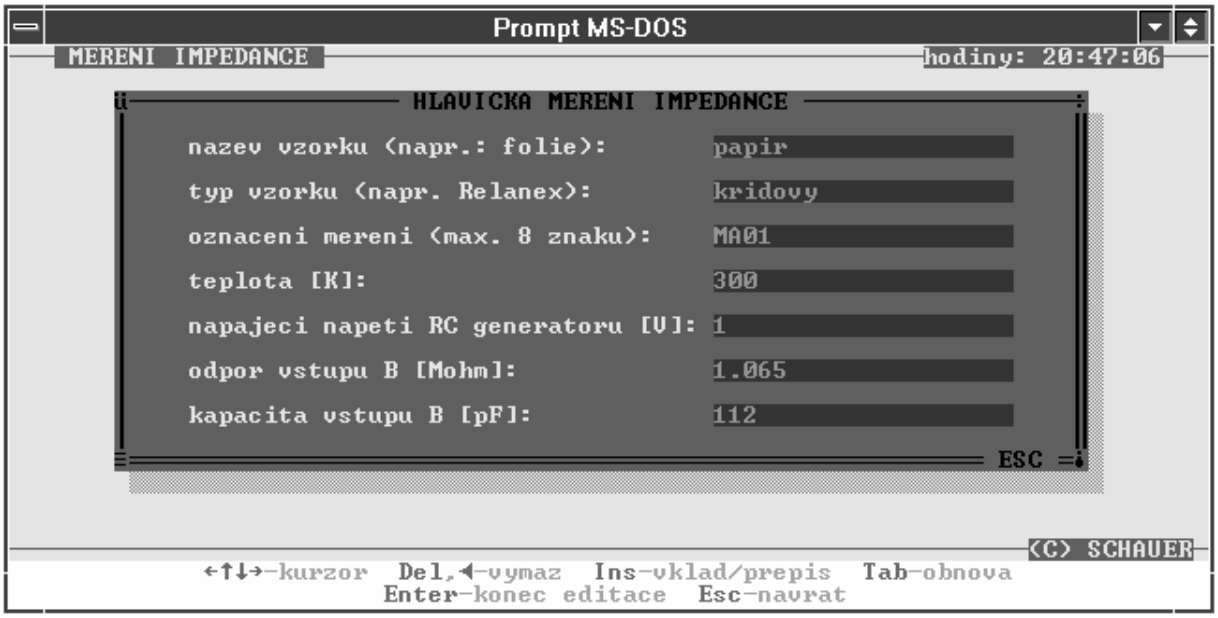

Figure 7: Items of measurement header are predefined in the file impedanc.ini and thus the measurement head is easy to fill in.

3.1.2 Measurement

Measurement starts by selecting ‘Measure’ from the main menu. The measurement results are stored in an output file with the same name as the measurement name in the header, but with the extension IMP. These files can be further processed by selecting ‘Processing’ in the main menu.

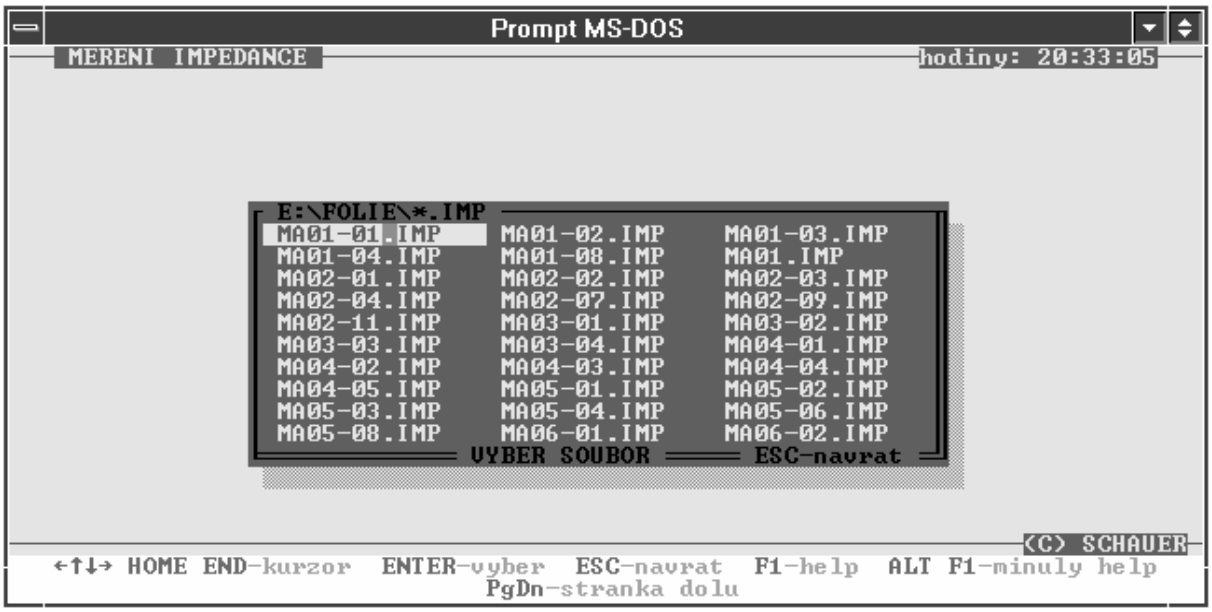

Figure 8: Clicking on the processing, the operator obtains a list of files with the extension IMP (files are the outputs from the measuring program - ready for further processing).

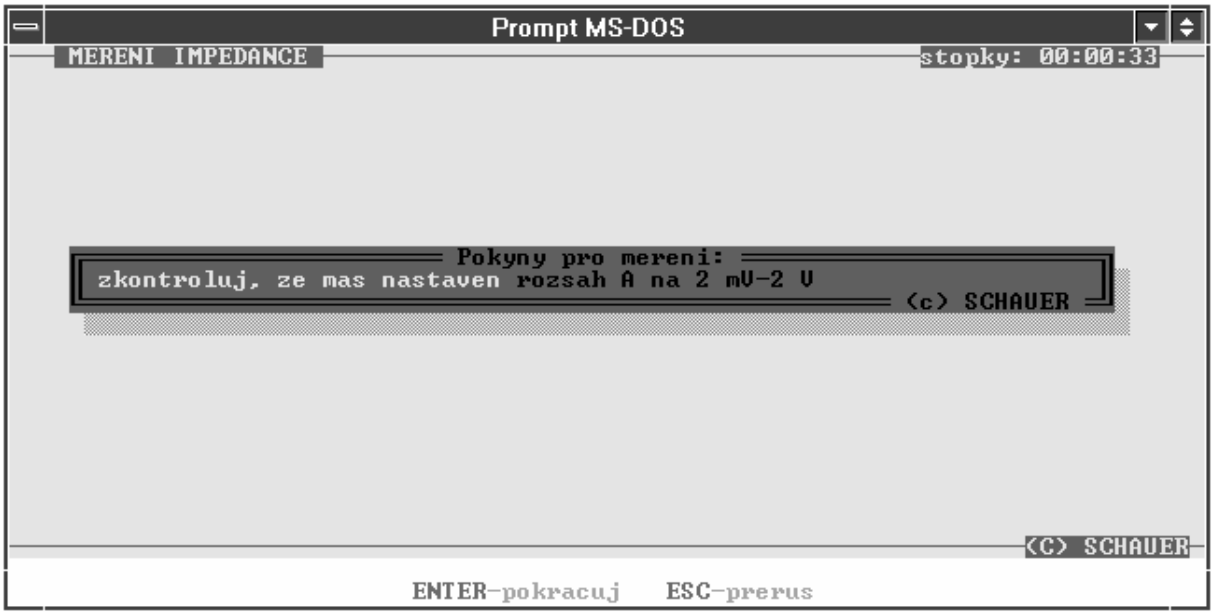

Figure 9: The operator is asked to control apparatus and instruments, during the measurement.

3.1.3 Processing

As shown in Figure 8, this operation offers a list of files with the extension IMP that are the output of our measurement program. These files are located in the working directory. We select one of the forms of evaluation. Then the process of impedance spectroscopy starts. Results are the set of tables and graphs $Z(f)$, Re$Z(f)$, Im$Z(f)$, tg $\delta(f)$, $R_p(f)$, $C_p(f)$, that we discussed in the theoretical part of this contribution.

4 CONCLUSION

Impedance spectroscopy of insulating layers based on monitoring the impedance characteristics of metal-insulator-metal (MIM) structures is a relatively fast, non-destructive testing method suitable for predicting the lifetime and reliability of insulating materials. The published method here is based on measurements of gain and phase shift on the AC voltage divider, which consists of the measured system MIM and of the known impedance. The most appropriate examined parameter of the insulating film is frequency dependence of loss-factor, or the frequency dependence of dielectric loss P.

Polarization dielectric losses are an important criterion for testing the quality and reliability of dielectrics, especially in power applications.

ACKNOWLEDGMENTS

This paper was supported by the Grant Agency of the Czech Republic, project number 102/94/0858.

REFERENCES

Kusak, I.: 2009. *Impedance Spectroscopy of Ceramic (Plain) Roofing Tiles*, International Interdisciplinary Technical Conference of Young Scientist Intertech 2009, ISBN Politechnika Poznan, Poznan, Poland.

Lunak, M.: 2009. *Non Destructive Testing of Cetris-Basic Wood-Cement Chipboards by Using Impedance Spectroscopy*, The 10th International Conference of The Slovenian Society for Non-Destructive Testing "Application of Contemporary Non-Desructive Testing in Engineering", Slovinsko Ljubljana.

Schauer, P.: 2001. *Transport and Noise properties of CdTe(Cl) Crystals*. Microelectronics Reliability, vol. 41, iss. 3, pp. 431-436.

Influences of Utility Networks on Measuring

V. Švehla *
Projekce elektro, Brno, Czech Republic
** Corresponding author: svehla@cronax.com*

DOI: 10.2478/v10158-010-0006-0

ABSTRACT: The measuring of any quantities is always encumbered with inaccuracy. To attain the best results it is necessary to restrict these errors. The exactness of measuring depends on the quality of the measuring equipment, the lay-out of the equipment, and on external influences. The goal of this paper is to draw attention to those external influences that are rare or are not supposed to be present.

KEY WORDS: Circuit, frequency, line, cable.

1 THE TEXT

Utility networks placed underground and in the air are used for the comfort of mankind. In cities and towns, these include, above all, water mains, sewerage systems, gas mains, and electricity mains, as well as the supply of railway applications for public transport. Utility networks placed in the air are used for connections and radio and television broadcasting. This paper deals with the influences of radio relay communication and the contact lines in Brno – Veveří.

1.1 Radio relay links

České Radiokomunikace are one of the radio relay links operators. A wireless connection is operated on frequencies from 1.5 to 40MHz. For operation on the above mentioned frequencies direct visibility between a transmitter and a receiver is necessary. To ensure a quality transmission the operator requires corridor lengthwise ideal beam axis. If a certain part of the energy of the beam is outside the corridor; its level is not suitable for quality reception, on top of which it can be a source of interference for other equipment. See the line in Figure 1.

1.2 Traction equipment

Public transport in Brno comprises both of tracked and untracked lines. In the case of tracked lines, the system of rail connected plus pole is used. Tractions are fed from rectifier substations, where alternating current is transformed to direct current. Trams and trolleybuses accept electrical current from contact line routes and rails that are connected by cables with rectifier substations. Tracks are fed in segments; these segments are electrically divided and fed by means of independent cables. Rectifier substations supply tracks in certain areas around the rectifier substation; it is for this reason that feed cables are placed in streets without transport. The feeding system is subject to continuous development. Formerly, trams were only fed by cables to the section of contact line routes.

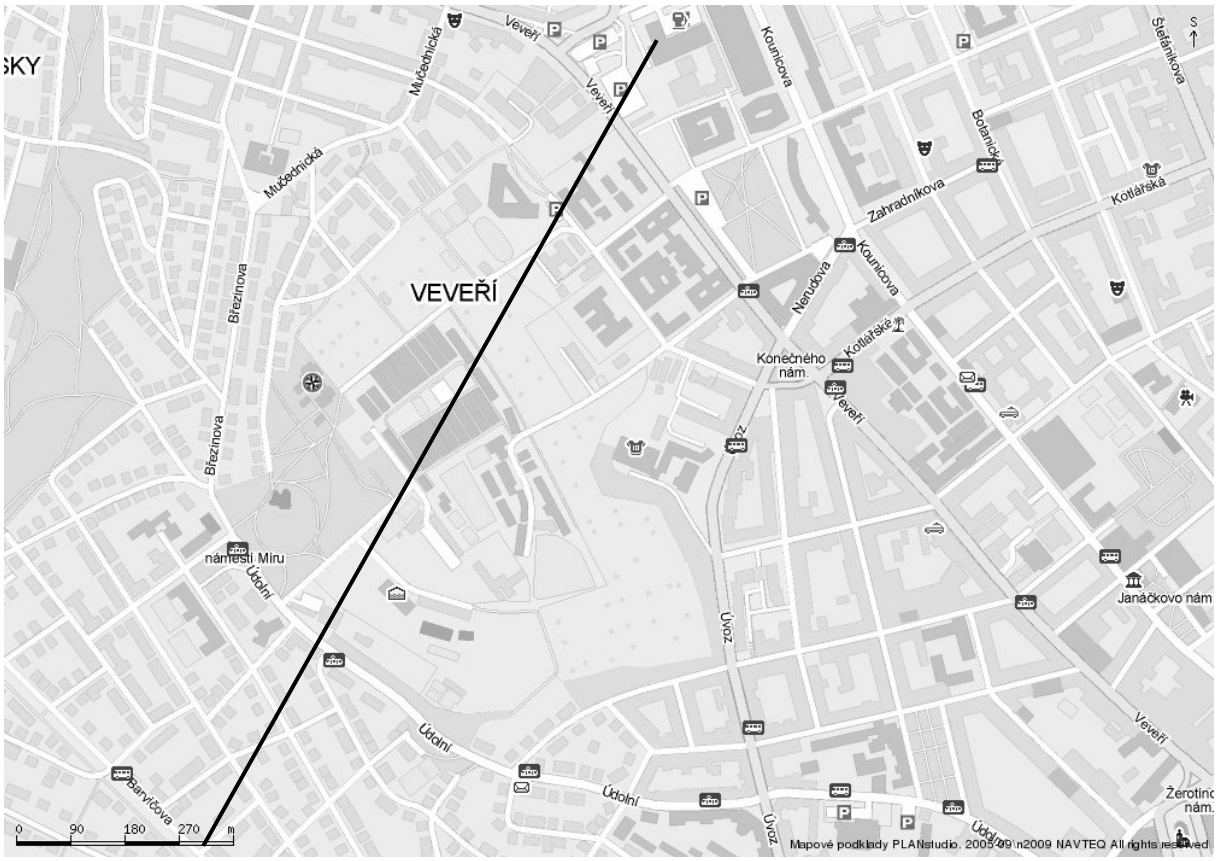

Figure 1: Radio-relay line Barvičova – Šumavská, Brno.

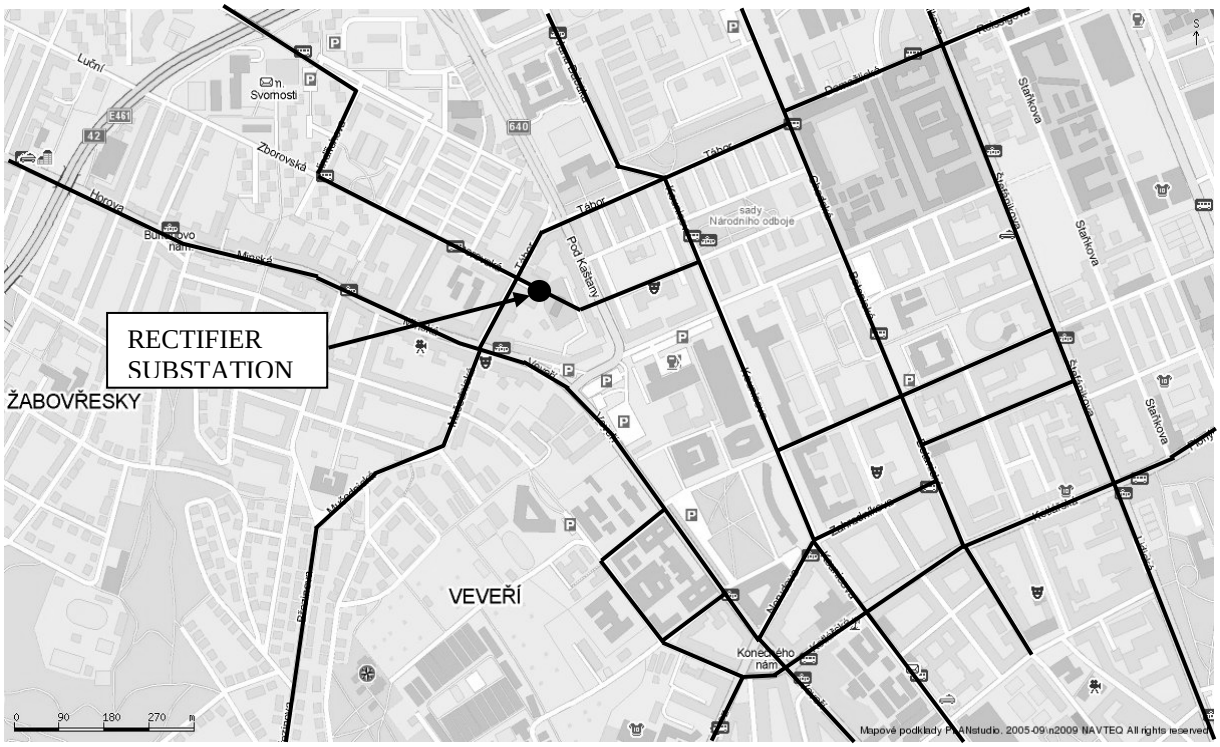

Figure 2: Traction equipment in Brno – Veveří.

Rails were only fed in the place that was close to the rectifier substation and electric current was led to all sections solely by rails. When trolleybuses were launched, feeding was connected to tram network, and the minus pole from the contact line route was connected to the contact line route without a switch, the rail was connected to the plus contact line route. Feeding by independent cables was established only in the sectors where trolleybuses went along streets without tram tracks. In some sectors with both tram and trolleybus transport, the tram contact line route was used for feeding trolleybuses. In the beginning this was convenient, but it had to be changed when TII trams were launched; this type required a higher volume of electrical current. At that time, a new system of rail feeding cables was introduced; each section has the same number of cables for both polarities. This process is in progress and has not been completed yet. Further changes are being carried out continuously; tram feeding and trolleybus feeding are being separated, which also has not been finalised yet. The goal of this process is to separate the tram feeding from trolleybus feeding, including the rectifying substations.

Brno – Veveří is fed mostly from the rectifying substation in Tábor (see Figure 2). This rectifying substation has, on the direct side, one system of bus bars fed by all rectifiers and this system is used for feeding trams and trolleybuses in this locality.

The section of tram track in Veveří street and along the Faculty of Civil Engineering VUT starts close to the cinema Lucerna and runs up to the crossroad Veveří – Kotlářská; it is 997m long – see Figure 3. Feeding from the rectifying substation Tábor is ensured by cables along Veveří, where two feed points are placed. One of the feed points is placed between the streets Mučednická and Šumavská and the second is placed in Rybkova, close to Veveří. Cables from the rectifying substation leading along Tábor street, turn into Veveří and than lead to the street Resslova. At this point, cables leave Veveří and lead along Resslova, Žižkova and Rybkova streets back to Veveří.

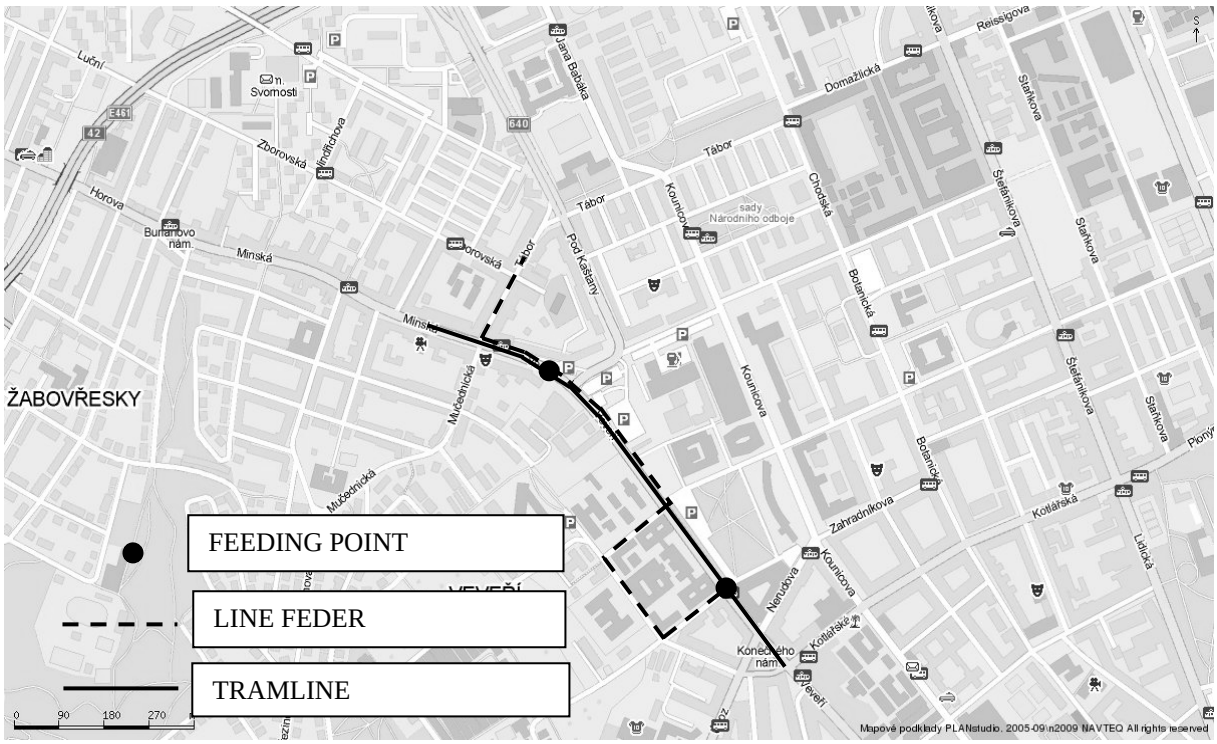

Figure 3: Tram-line Veveří.

Between feed points, a part of electrical current goes through the feeding cables, and a part goes through the contact line route and rails. For the minus pole, 37% goes through the contact line route and 63% goes through the feeding cables. For the plus pole, 87% goes through the rails and 13% goes through the feeding cables. The total maximum current in the above mentioned section

Reaches 2400A, according to measurements. In the section between streets Kotlářská and Nerudova, 853 regular tramways operate between 4.57 to 22.49 on weekdays. The heaviest period of traffic occurs between 7 a.m. and 8 a.m. with a total of 69 trams. The amount of necessary electrical current is influenced by two traffic lights and by the types of trams going through the section.

The section of trolleybus track in the street Kounicova and along the University of Defence starts between streets Tábor and Klusáčkova and goes to the crossroad Kounicova Zahradníkova and is 729m long – Figure 4. Feeding is placed solely at the stop Klusáčkova. Cables are placed according to the shortest possible way from the rectifying substation and both polarities are parallel. 492 trolleybuses go through this section every day and the maximum needed electrical current reaches 690A.

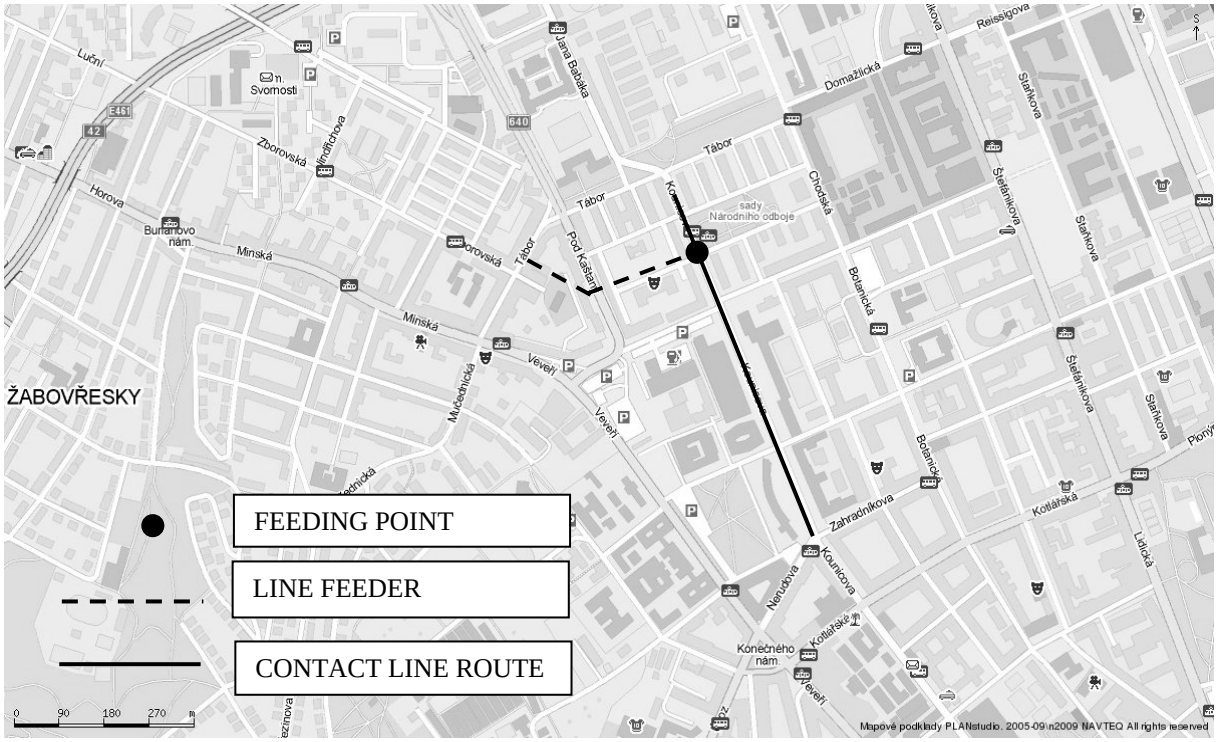

Figure 4: Trolley-bus line Kounicova.

The trolleybus track Úvoz – Kotlářská (see Figure 5) is fed from two rectifying substations - Tábor and Údolní. For feeding from the rectifying substation Tábor, a minus cable is placed up to feeder in Úvoz. The plus pole is connected to cables for the tram feeding in Veveří from the distribution box in Rybkova. The current consumption in Úvoz ranges from 600A to 1200A.

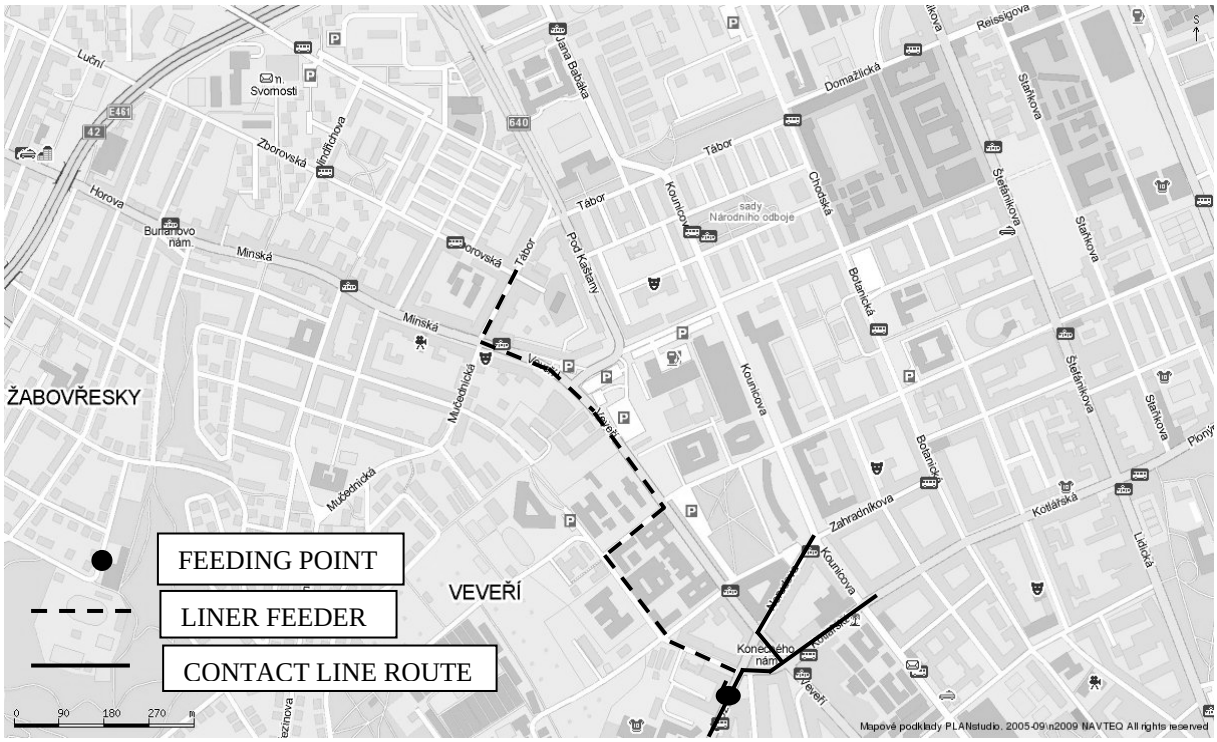

Figure 5: Trolley-bus line Úvoz Kotlářská.

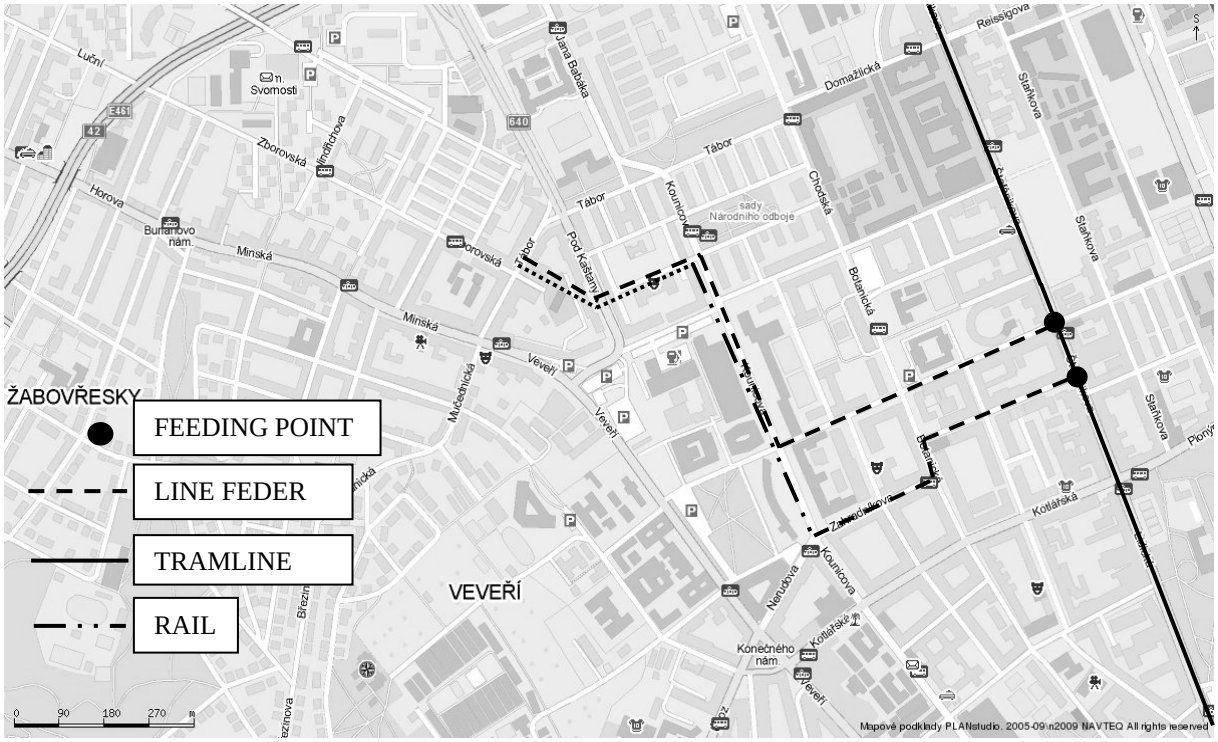

Figure 6: Tram-line Štefánikova.

The tram track in Štefánikova – see Figure 6 is fed from the rectifying substation in Tábor and from another one in the city centre. The cables for the minus pole are placed concurrently with cables for feeding traction in Kounicova and the stop Klusáčkova; they than turn to Kounicova street in the direction to the city centre and later to Šumavská. There is a feed point for the tram contact line route. The plus pole is carried from the rectifying substation

to the tram rails in Kounicova in the area of the tram stop Klusáčkova. Subsequently, the electric current goes through the tram rails up to the crossroad Kounicova – Zahradníkova. There the cables are connected to the rails; these cables are placed along the streets Zahradníkova, Botanická and Dřevařská up to the tram track rails in Štefánikova. The electric current consumption ranges from 300A to 1500A.

The return circuit for the plus pole (see Figure 7) utilizes the contact line routes, rails and return conductors. The individual sections are not divided by section insulators; they constitute one large system with more feeding cables.

There are, besides the direct current, elements of alternating current in the supply network. These are network frequency 50Hz, and the frequency of unfiltered rectifying 300 Hz. Further sources of various frequencies comprise of static converters, rectifiers, traction trains regulators, etc. The contact of current collectors and contact line routes are a source of irregular disturbance. This source strongly depends on temperature and air humidity. Freezing ice on contact line routes can cause serious problems.

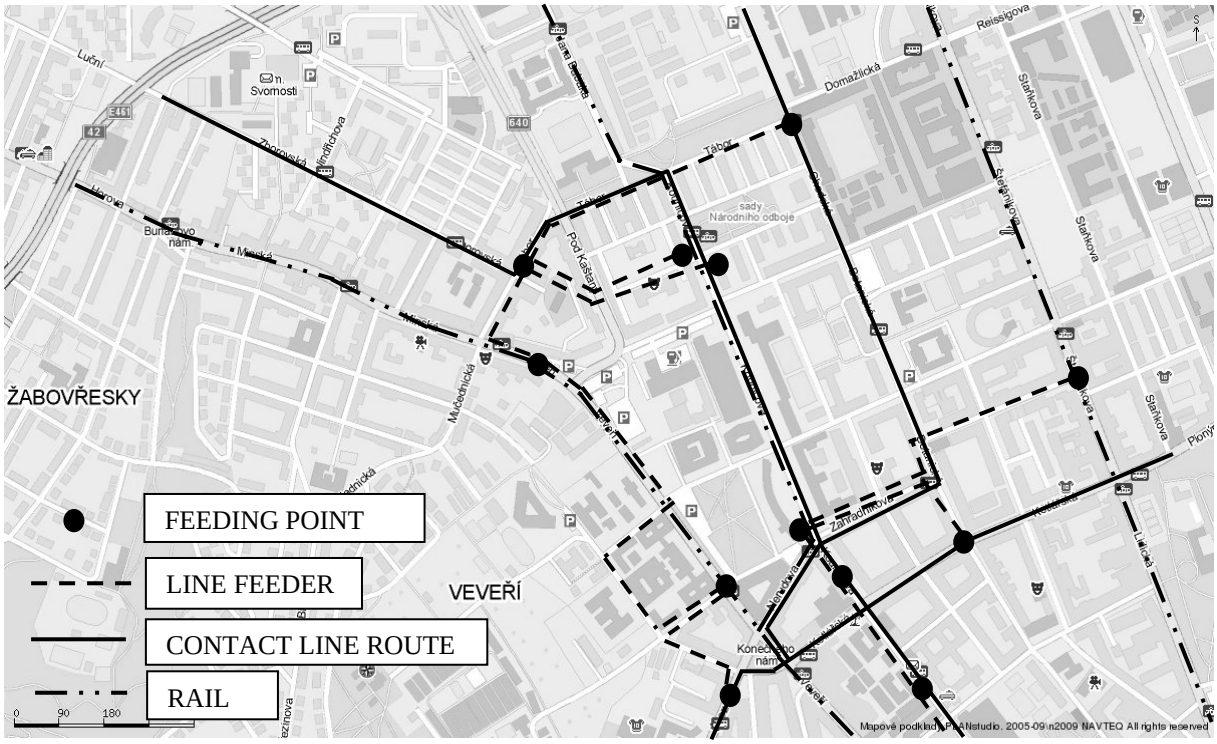

Figure 7: Return cables in Veveří.

REFERENCES

Řihák, z. a kol., 1993. *Studie stavby mrakodrapu Šumavská Brno.*

Šebor, J., 2008. *Napájecí síť.* Dopravní podnik města Brna.

Atelier CREO sro., 2006. *Kabely DPmB - Žižkova – project.*

Atelier CREO sro., 2009. *Kabely DPmB – Tábor – Klusáčkova.*

www.mapy.cz

Pedestrian Model for Injury Prediction for Lateral Impact

H. Čechová * & L. Hynčík
New Technologies - Research Centre in the Westbohemian Region, University of West Bohemia, Plzeň, Czech Republic
** Corresponding author:hcechov@ntc.zcu.cz*

DOI: 10.2478/v10158-0007-z

ABSTRACT: World-wide statistics still reflect a high percentage of seriously injured pedestrians in the urban areas. The lateral impact is the most common type of traffic accident in towns. This paper describes the validation of a pedestrian model that will be able to assess the type and level of injury. The human model used is rigid body based with realistic biomechanical joints. The human body model is validated for the case of a lateral pedestrian impact using published experimental cadaveric data. Particular body segment trajectories fit into given kinematic corridors. Based on the standard injury criteria the pedestrian model is able to predict life threatening risk.

KEY WORDS: Biomechanics, virtual human model, pedestrian impact.

1 INTRODUCTION

Walking is the most natural way to get from one point to another. As stated by the European Commission around 17% of all traffic fatalities in EU countries are with pedestrians. Based on the study (Maňas et al. 2009) pedestrians in the Czech Republic belong to a group of the most at risk vulnerable road users. The above mentioned study also summarizes that pedestrian road accidents are the most frequent in urban areas with a passenger car impact velocity up to 50km/h. Pedestrian protection is therefore still an important topic, as is also shown in the study of Obermann & Kovanda (2009).

In his article, Ishikawa et al. (1993) analyzes possible pedestrian impact scenarios and summarizes that the most frequent accident type corresponds to a lateral impact when a pedestrian is crossing the road.

The limited biofidelity of dummy models and, especially the actual tendency towards human models legalization (Haug et al. 2003) are the driving force for the creation of correct human body models. The aim of this study is to obtain a validated pedestrian model able to give the overall injury analysis and able to serve for the improvement of safety components in means of traffic.

The used human model Robby (Hynčík, 2001) belongs to a family of Human Articulated Rigid Body (HARB) models (Haug et al. 2004) developed on the PAM computational platform (PAM-System, 2009). The model consists of rigid bodies separated into segments connected by biomechanical joints (Robbins, 1983).

2 METHOD

2.1 External experimental background

The model is validated using both literature sources (Ishikawa et al. 1993; Kerrigan et al. 2005; Simms & Wood, 2006; Stammen & Barsan-Anelli, 2001) involving experiments with PMHS (Post Mortem Human Subject) and dummies, and also, in several cases, using computer simulations of performed tests. As a key source the work of Kerrigan et al. (2005), presenting the detailed description of the experiment with a full-scale pedestrian impact, is chosen.

The pedestrian in the mid-stance phase of a gait cycle is positioned laterally in front of the car. This position is the most characteristic of real pedestrian collisions and, moreover, represents a significant part of the normal gait cycle (Kam et al. 2005). The mid-stance is the period of the gait between the first contact of the front leg (heel strike) and the last contact of the rear leg (toe off) with the ground. It occupies the period from 7% to 32% of the gait cycle. The test was realized three times with cadavers and then with a Polar II Dummy with an impact speed of 40km/h (11 m/s). The experimental corridors for body segment trajectories scaled to 50 percentile male were established and the head velocity corridors were published. The analysis was focused only on the primary impact which is limited by the first contact of the car and the pedestrian and the head strike to the windscreen.

2.2 Impact scenario setup

The original Robby model of an average male (Robbins, 1983) is used. The Robby is 174 cm tall and he weighs 74 kg. The relative position of the car and the pedestrian is set according to the experiment (Kerrigan et al. 2005). It means that Robby in the mid-stance phase of the gait cycle is standing laterally to the car front with the struck limb in front, see Figure 1. The hands are connected together ahead of the body to restrict their influence on the body kinematics during the crash.

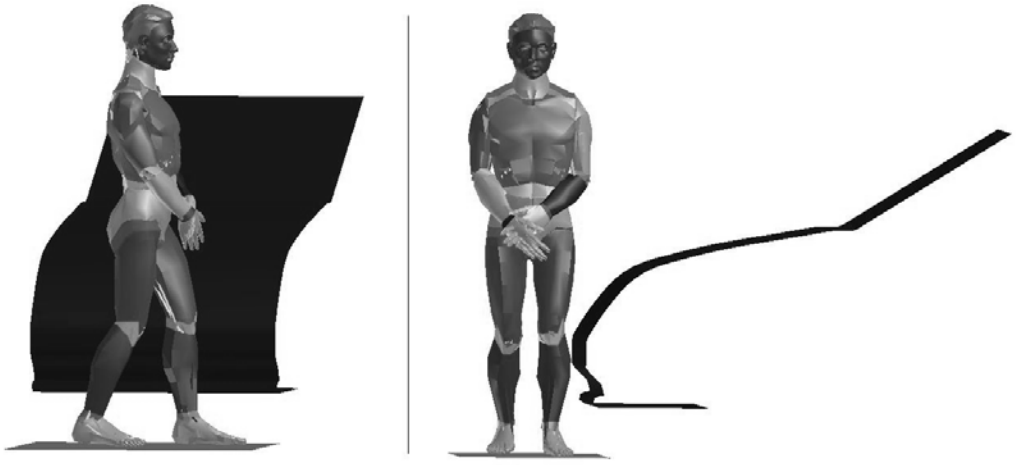

Figure 1: Pedestrian impact model, starting position.

Main car characteristics significantly influencing the seriousness of the pedestrian injury are the mass, the face geometry, and the stiffness. The car profile geometry is adapted from Kerrigan et al. (2005). Despite the precise description of the test itself, the publication lacks detailed information about the car material characteristics. Hence additional literature

sources (Simms & Wood, 2006; Stammen & Barsan-Anelli, 2001) are used to complete the model parameters. The car is modeled as rigid with parameters defined according to a real small car, as reported in Table 1. The Robby's friction coefficient with the ground is set to 0.65, and with the car structure to 0.25 according to Ishikawa et al. (1993).

Table 1: Table of used car parameters, adapted from (Simms & Wood, 2006).

m [kg]	I_{xx} [kg mm^2]	I_{yy} [kg mm^2]	I_{zz} [kg mm^2]
1200	425e+6	1933e+6	2020e+6

A special contact type, including the stiffness characteristics of real car material properties, is used (PAM-System, 2009). It enables the simulation of a more realistic impact behavior of rigid bodies. The used bonnet and windscreen characteristics displayed in Figure 2 are adapted from (Simms & Wood, 2006).

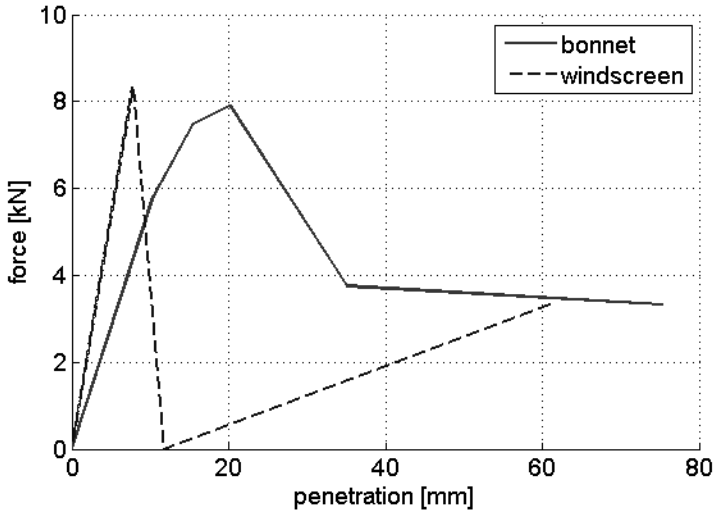

Figure 2: Car force penetration dependency, adapted from (Simms & Wood, 2006).

3 RESULTS AND DISCUSSION

3.1 Kinematics

The model kinematics is compared to the published experiments (Kerrigan et al. 2005). The car impacts the pedestrian at knee level, gathers him, and his body slides on the bonnet till the head hits the windscreen; at this instant both the computation and the experiment are stopped. The sequence of the pedestrian motion with the time step 20 ms is shown in Figure 3. The front struck limb tends to turn the model back, which was also proved by Kam et al. (2005). The body parts trajectories in the plane of the vehicle motion lie within the experimental corridors as can be seen in Figure 4 and Figure 5. The head velocity also fits in the experimental corridors, as shown in Figure 6.

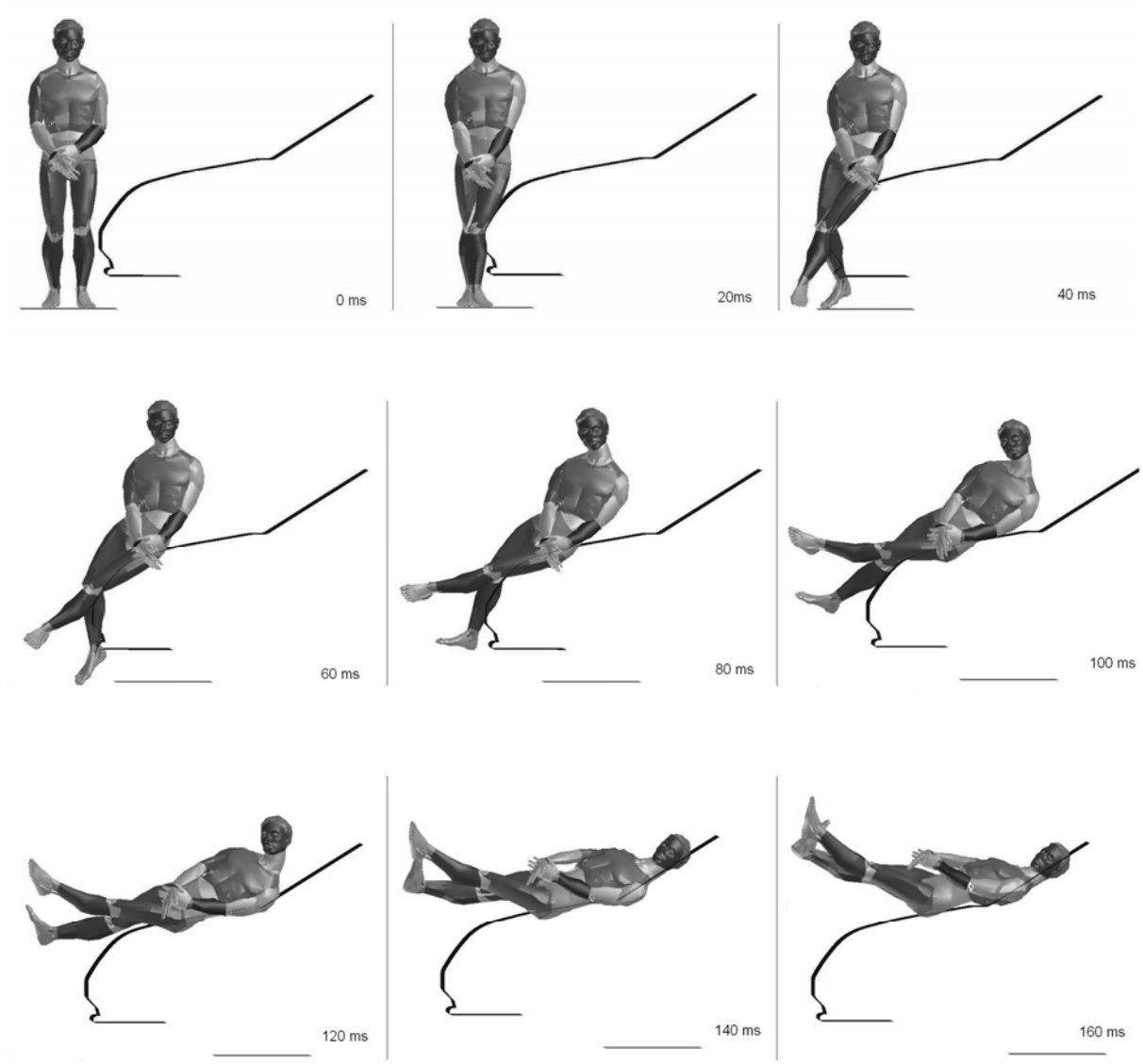

Figure 3: Time sequence of the impact simulation.

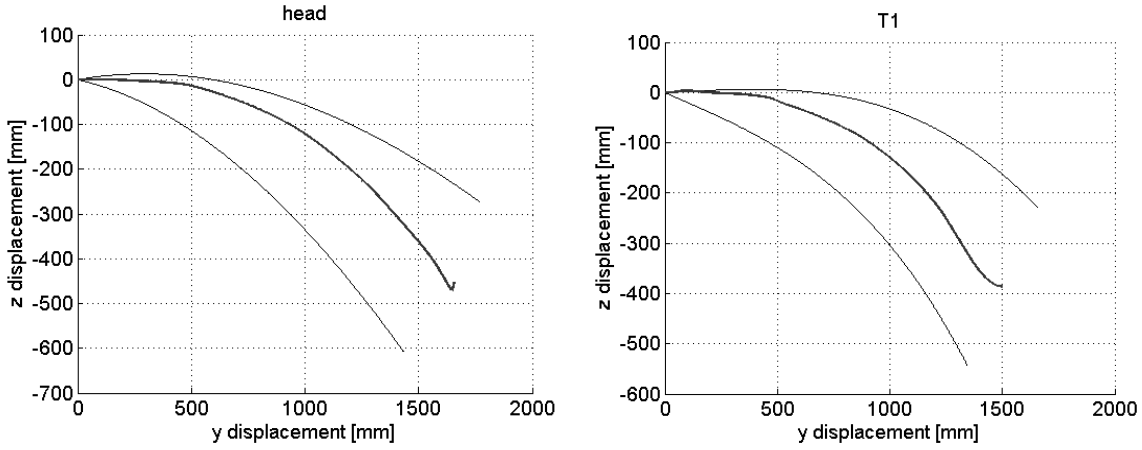

Figure 4: Trajectories of the head (left) and the T1 vertebra (right) in the experimental corridors (black lines) in the mediolateral plane.

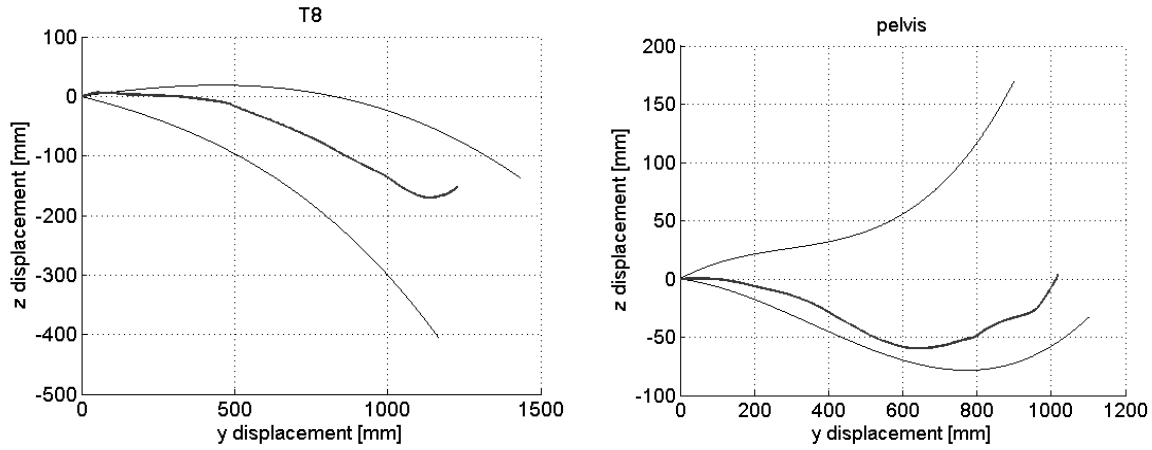

Figure 5: Trajectories of the T8 vertebra (left) and the pelvis (right) in the experimental corridors (black lines) in the mediolateral plane.

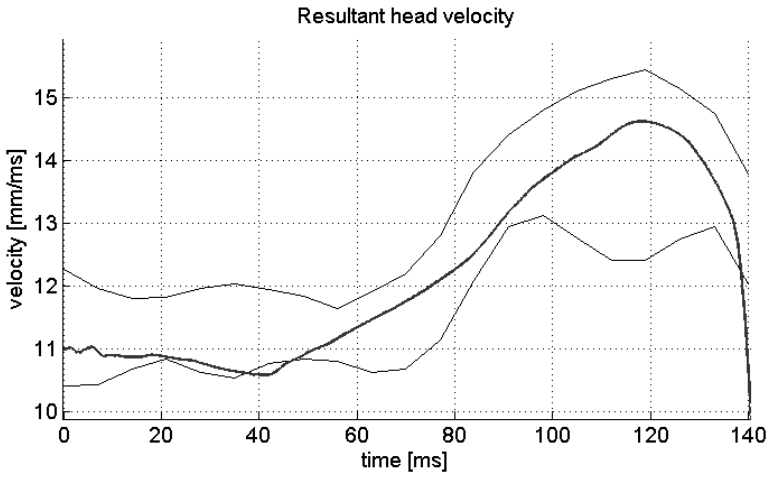

Figure 6: Head resultant velocity in the mediolateral plane in comparison with the experimental corridors (black curves).

3.2 Injury prediction

With regard to the successful kinematic model validation a degree of pedestrian risk can be predicted in the sense of directory information. Since Robby is a rigid body based model, injury criteria based on body parts accelerations are used. Despite being highly simplified, they perform an adequate estimation of injury level and their development results from many experiments (Schmitt, 2004).

The standard head injury criterion HIC_{36} is applied. It performs the 50% risk of skull fracture that is qualified as AIS $\geq$ 2 (Schmitt, 2004). The thorax injury is estimated using the 3ms criterion indicating the 25% risk of AIS $\geq$ 4 (Schmitt, 2004). The pelvic peak acceleration for pelvis fracture is 73 g as reported by Zhu et al. (1993). This criterion was derived from side impact with cadavers and it is also used by Simms & Wood, (2009) to indicate the pedestrian pelvic injury. The knees, especially in the case of a side impact,

are under threat of bending. The maximum mediolateral bending angle according to van Rooij, (2003) is around 13 degrees.

Table 2: Injury analysis.

	HIC_{36} [-]	3ms [g]	Pelvis [g]	Knee bending angle [deg]	
				Right leg	Left leg
Injury limit	1000	60	73	± 12.7	± 12.7
Robby 40km/h	1483	66	80.6	26, -41	14, -57

All tested injury criteria and their limit values are summarized in Table 2. It is obvious that the tested criteria exceed their limits. Figure 7 demonstrates the knees' movement during the impact and the confrontation with the limit values. In conclusion, the pedestrian suffers serious injuries in all controlled body parts.

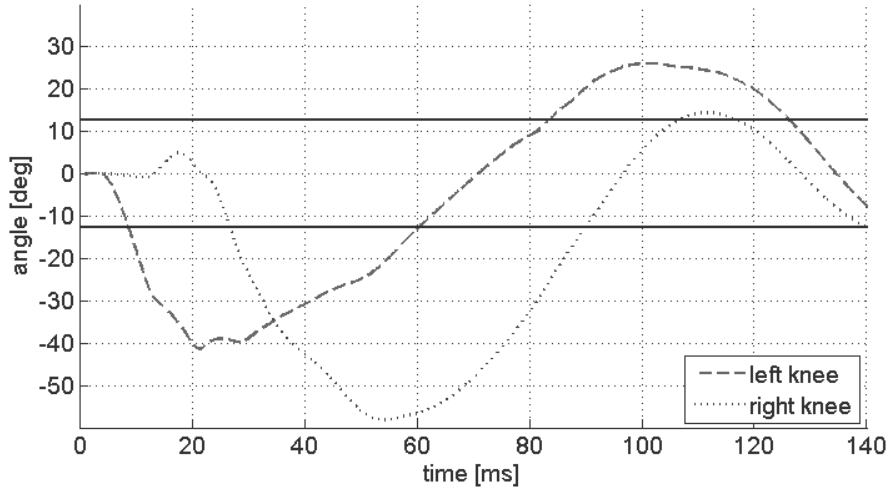

Figure 7: Pedestrian knee bending angles (dashed and dotted line) during the lateral impact and the injury limits (solid lines).

4 CONCLUSION

The previously developed rigid body based human model is validated in the full-scale pedestrian impact. Simulation results are compared to published cadaveric experimental data. Real car characteristics, including a detailed car profile, are used. All monitored body segments trajectories fall within the experimental corridors.

Despite the injury values only giving a general indication of the severity rather than a precise injury prediction, they perform as an appropriate tool in the case of rigid body based models. The presented injury analysis of the lateral impact in relatively low velocity (40 km/h) indicates the serious pedestrian injuries to the head, thorax, pelvic area, and both knees.

ACKNOWLEDGEMENT

The work is supported by the project CG911-044-150 of the Czech Ministry of Transport and by the John H. and Amy Bowles Lawrence Foundation. Great thanks belong to ESI Group International.

REFERENCES

Haug, E., Beaugonin, M., Montmayeur, N., Marca, C., Choi, H.: 2003. *Towards legal virtual crash tests for vehicle occupant safety design using human models*. International Crashworthiness and Design Symposium (ICD03).

Haug, E., Choi, H.Y., Robin, S., Beaugonin, M.: 2004. *Human models for Crash and impact simulation.* Special volume of Handbook of numerical analysis, Vol. XII, (Editor P.G. Ciarlet) Elsevier, North Holland, pp. 231-670.

Hynčík L.: 2001. *Rigid Body Based Human Model for Crash Test Purposes.* Engineering Mechanics, Engineering Academy of the Czech Republic, Vol. 8, No. 5, pp. 1-6.

Hynčík, L., Nováček, V., Bláha, P., Chvojka, O., Krejčí, P.: 2007. *On scaling of human body models*. Applied and Computational Mechanics, University of West Bohemia, Pilsen, Vol. 1, No.1, pp. 63-74.

Hynčík, L., Číhalová, L., Kocková, H., Bláha, P., Beaugonin, M.: 2009. *Virtual anthropometric human models for safety*. Proceedings of International Society of Biomechanics, Cape Town, South Africa, 2009.

Ishikawa, H., Kajzer, J., Schroeder, G.: 1993. *Computer Simulation of Impact Response of the Human Body in Car-Pedestrian Accidents*. Paper No. 933129, Thirty-seventh Stapp Car Crash Conference Proceedings.

Kam, C. Y., Kerrigan, J., Meisser, M., Drinkwater, C., Murphy, D., Bolton, J., Arregui, C., Kendall, R., Ivarsson, J., Crandall, J., Deng, B., Wang, J. T., Kerlinge, Hahn, W.: 2005: *Design of a Full-Scale Impact System for Analysis of Vehicle Pedestrian Collisions*. Paper 2005-01-1875, Society of Automotive Engineers, Warrendale, PA.

Kerrigan, J. R., Murphy, D. B., Drinkwater, D.C., Kam, C.Y., Bose, D., Crandall, J.R.: 2005. *Kinematic corridors for PMHS tested in full-scale pedestrian impact*. University of Virginia Center for Applied Biomechanics, paper No. 05-0394.

Maňas J, Glac, V, Šefrhans, M.: 2009. *Analýza dopravní nehodovosti za účasti zranitelných účastníků dopravy*. Zpráva k řešení aktivity A 901 dílčího cíle DC 01 projektu Ministerstva dopravy č. CG911-044-150. MECAS ESI s.r.o., Plzeň.

Obermann, J., Kovanda, J.: 2009. Pedestrian Detection. Transactions on Transport Sciences, Ministry of Transport of the Czech Republic, Vol. 2, No. 3, pp. 128 - 133.

PAM-System Users Manual, Version 2009.

Robbins, D. H.: 1983. *Anthropometric Specifications for Mid-Sized Male Dummy, Volume 2*. University of Michigan Transportation Research Institute (UMTRI), research report number UMTRI-83-53-2.

van Rooij, L.: 2003. The evaluation of the kinematics of the MADYMO human pedestrian model against experimental tests and the influence of a more biofidelic knee joint. 5th MADYMO Users Meeting of the Americas.

Schmitt, K. U., Niederer, P., Walz, F.: 2004. *Trauma Biomechanics, Introduction to Accidental Injury*. Springer-Verlag, Germany.

Simms, C. K., Wood, D. P.: 2006. *Pedestrian risk from cars and sport utility vehicles – a comparative study*. Proc. IMechE, Vol. 220 Part D: J. Automobile Engineering.

Simms, C. K., Wood, D. P.: 2009. *Pedestrian and Cyclist Impact, A Biomechanical Perspective*. Springer Science+Business Media, B.V.

Stammen, J., Barsan-Anelli, A.: 2001. *Adaptation of a human body mathematical model to simulation of pedestrian/vehicle interactions.* 4th MADYMO User's Meeting Of The America's, Detroit.

Zhu, J. Y., Cavanough, J. M., King A., I.: 1993. *Pelvic biomechanical response and padding benefits in side impact based on cadaveric test series*. SAE paper 933128.

European Commission – Road Safety:
http://ec.europa.eu/transport/road_safety/users/pedestrians/index_en.htm

Instructions to the autors

1 GENERAL GUIDELINES

Papers based on accepted abstracts and prepared in accordance to these guidelines are to be submitted through the journal's web site www.transportsciences.org.

All papers, using Microsoft Word2000 (or newer) are **limited to a size of at least 4 and no more than 8 single-spaced pages** on A4 paper size (297 mm X 210 mm), including figures, tables, and references and should have an **even number of pages**. The paper's top, bottom, right and left margins must be 2.5 cm. No headers, footers and page numbers should be inserted.

2 TITLE, AUTHORS, AFFILIATIONS

The title of the paper must be in title letters, Times New Roman, font size 16, and aligned left. Use more than one line if necessary, but always use single-line spacing (without blank lines).

Then, after one blank line, aligned left, type the First Author's name (first the initial of the first name, then the last name). If any of the co-authors have the same affiliation as the first author, add his/her name after an & (or a comma if more names follow). In the following line type the institution details (Name of the institution, City, State/Province, Country and e-mail address of a corresponding author). If there are authors linked to other institutions, after a blank line, repeat this procedure.

The authors name must be in Times New Roman, regular, and font size 12. The institution details must be in Times New Roman, *italic*, and font size 10.

3 ABSTRACT

The abstract should start after leaving eight blank lines. Type the text of the abstract in one paragraph, after a space behind the word abstract and colon, with a maximum of 250 words in Times New Roman, regular, font size 12, single-spaced, and justified. After leaving one blank line, type KEY WORDS: (capital letters, Times New Roman, font size 12), followed by a maximum of five (5) key words separated by commas. Only the first letter of the first key word should be capitalized.

4 THE TEXT

The main body of the paper follows the key words, after two blank lines (i.e., two blank lines between the first heading and the key words). The body text should be typed in Times New Roman, font size 12 and justified. The first line of the paragraphs should be indented 5 mm except the paragraphs that follow heading or subheading (i.e., the first line of the paragraphs that follow heading or subheading should not be indented). Never use bold and never underline any body text.

4.1 HEADINGS AND SUBHEADINGS

The headings are in capital letters, Times New Roman, font size 12. Subheadings are in title letters Times New Roman, font size 12. The headings and subheadings must be aligned left and should not be indented.

Leave two blank lines before and one after the heading. There should be one (1) blank line before and after the subheadings. All headings and subheadings must be numbered.

If a heading or subheading falls at the bottom of a page it should be transferred to the top of the next page.

4.2 FIGURES AND TABLES

Figures, line drawings, photographs, tables should be placed in the appropriate location, aligned centre, and positioned close to the citation in the document. They should have a caption, Times New Roman font size 12, with a colon dividing the figure number and the title (Figure 1: Material properties) and should be numbered consecutively, e.g. Figure 1, Figure 2, Table 1, and Table 2.

4.3 REFERENCES

At the end of the paper, list all references with the last name of the first author in alphabetical order, underneath the heading REFERENCES, as in the example. The title of the referred publication should be in italic while the rest of the reference description should be in regular letters. References should be typed in Times New Roman font size 12. citation standard ISO 690.

More details can be found at **www.transportsciences.org**.

TRANSACTIONS ON TRANSPORT SCIENCES

Volume 3 2010 Number 1

CONTENTS